Combustion and Flame 173 (2016) 161–178

Contents lists available at ScienceDirect

Combustion and Flame

journal homepage: www.elsevier.com/locate/combustflame

Application of unstrained flamelet SGS closure for multi-regime premixed combustion

Ivan Langella[a,*], Nedunchezhian Swaminathan[a], Robert W. Pitz[b]

[a] Department of Engineering, University of Cambridge, Cambridge CB2 1PZ, UK
[b] Mechanical Engineering Department, Vanderbilt University, Nashville, TN, USA

ARTICLE INFO

Article history:
Received 15 January 2016
Revised 29 August 2016
Accepted 30 August 2016
Available online 12 September 2016

Keywords:
Bluff-body premixed flames
SGS variance
SDR
Unstrained Flamelet
LES

ABSTRACT

Large eddy simulation of turbulent premixed combustion behind a bluff-body is performed using unstrained flamelet model with a presumed probability density function to calculate filtered reaction rate. The subgrid variance of the progress variable required in this approach is calculated using its transport equation to include contributions from reaction, turbulence and molecular diffusive and dissipative processes at sub-grid scales. The dissipation rate of the variance is obtained using an algebraic closure, which maintains physical consistency among turbulence, reaction and molecular diffusion. Various quantities such as mean velocity, temperature and species mass fractions computed for two bluff-body flames experiencing 2% and 24% turbulence intensities are compared to their respective measurements. These comparisons are very good suggesting that the unstrained flamelet SGS closure works well for multi-regime combustion. The demonstrated success of this modelling framework is explained on a physical basis.

1. Introduction

The use of a bluff-body is common in practical combustors because the recirculation zone containing hot products behind the bluff-body provides a simple mechanism for flame stabilisation. Despite the simple geometry, the physical processes encompass strong interplay among turbulent transport, combustion and molecular diffusion. The shape and size of the recirculation zone influence the performance of these burners in general and the fluid dynamic attributes are governed by the bluff-body geometry, turbulence level and equivalence ratio at the burner inlet.

Large eddy simulation (LES) has the potential to capture these effects including transients such as local extinction and flame blow-off. Typical LES resolves dynamic scales of turbulence and scalar fields explicitly up to a cut-off scale, Δ, and the remaining sub-grid scale (SGS) phenomena are modelled. Turbulent premixed combustion is usually a SGS phenomenon and it needs to be modelled. This modelling must include the strong interplay among turbulent transport, heat release effects and molecular diffusion. Thus, developing a robust and accurate model for SGS premixed combustion is challenging and a number of approaches have been proposed in the past which are reviewed in [1,2]. The simplest of these approaches is the flamelet approach which has been applied successfully in many past studies, see [1–3] for a broad review. This approach has also been advanced to include additional complexities, for example dual-mode, non-premixed and premixed, combustion [4] and flame stretch effects [5]. However, the unstrained flamelet for SGS combustion closure can work well if various sub-models used in this closure are consistent with each other on a physical basis [6]. Thus, the objective of this study is to test its applicability for multi-regime turbulent premixed combustion established behind a bluff-body.

The combustion behind a triangular shaped bluff-body in a rectangular channel, commonly known as Volvo experiment [7,8], has been investigated using LES with various SGS combustion closures in the past, for example see [9–14]. Oblique turbulent premixed flames of propane–air mixture propagated in rectilinear geometry in the Volvo experiment, which is different from the flame considered for this study.

The bluff-body methane–air flame considered here is cylindrical and was investigated experimentally [15–19] and numerically [20–22] in the past. Hu & Correa [20] simulated this methane–air flame using Perfectly Stirred Reactor (PSR) model involving mixture fraction and a residence time in their 2D axisymmetric computation to cater for the distributed combustion. This flame was also computed using RANS and RANS/PDF approaches [23–28]. It has also been simulated using LES with a PDF SGS model [29],

* Corresponding author.
E-mail address: il246@cam.ac.uk (I. Langella).

http://dx.doi.org/10.1016/j.combustflame.2016.08.025

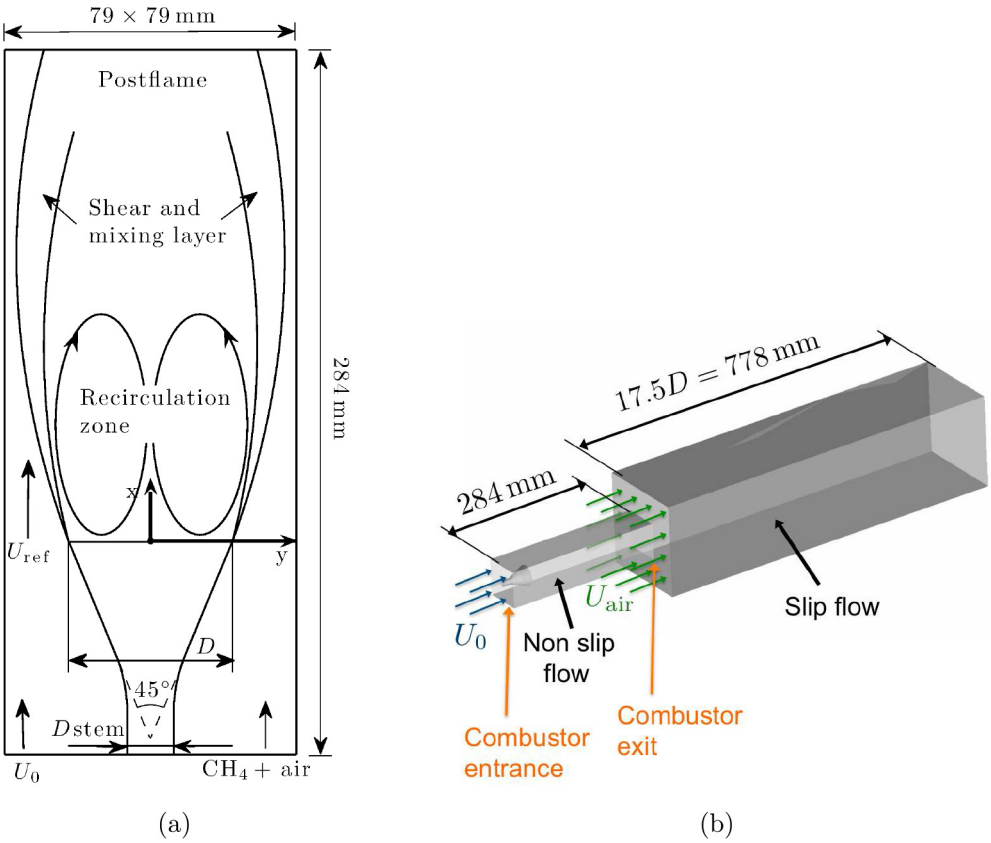

Fig. 1. Schematic of (a) experimental burner and (b) its computational model ($U_0 = 15$ m/s, $U_{air} = 0.2$ m/s).

linear eddy model [21], and turbulent flame speed models available in FLUENT and OpenFOAM packages [22].

All of the above works used only a small subset of measurements for the respective model validation and it appeared that advanced models were needed to capture the multi-regime combustion ranging from the corrugated-flamelets to distributed combustion regime [15–17]. Thus, it is quite challenging for a single combustion closure to capture this varied regime combustion. Specifically, the unstrained flamelet closure is of interest for this study and the aim is to test this closure for the multi-regime combustion because this closure has been shown [6] to work well for the flamelets regime combustion. Thus, its behaviour for distributed combustion regime is of particular interest for this study. It could be quite contentious to use the unstrained flamelet closure for distributed combustion regime in the classical viewpoint but earlier studies [30–35] have shown the presence of flamelets in distributed or broken reaction zones regime combustion. Thus, this regime of turbulent combustion can be seen as a situation in which locally thin laminar flames (flamelets), with their internal structures unperturbed by turbulent eddies, are distributed over a wider region yielding a thicker and more diffusive flame brush compared to the classical flamelet regime. The flame brush is the time- or ensemble-averaged structure resulting from these flamelets. Hence, it is worthwhile to explore the applicability of the unstrained flamelet closure but one must, as noted earlier, carefully maintain physical consistency among various sub-models used in this approach.

This paper is organised as follows. The next section describes briefly the bluff-body burner used here along with its experimental procedure. The LES model, SGS closures, numerical method and grid used, and boundary conditions employed are described in Section 3. The results are discussed subsequently and the conclusions are summarised in the final section.

2. Experimental case

The bluff-body configuration studied experimentally in [15–19] is chosen for this study and is shown in Fig. 1 along with its computational model. A methane–air mixture at 294 K having an equivalence ratio of $\phi = 0.59$ entered the combustion chamber having a dimension of $79 \times 79 \times 284\,mm^3$. The bluff-body had a base-diameter of $D = 44.45$ mm, stem-diameter of $D_{stem} = 12.7$ mm and an apex angle of $\theta = 45°$. It was placed at the centre of a duct which also formed the combustion chamber downstream of the bluff-body as shown in Fig. 1. A turbulence generator having 3.46 mm diameter holes was placed at about 58 mm upstream of the bluff-body base and the flow entering the combustor section had a bulk-mean velocity of $U_{ref} = 15$ m/s and turbulence intensity (TI), measured at $r/D = 0.55$ at the location of bluff-body base, of 2% or 24% (two flames) as described in [15–17]. The turbulent Reynolds number at the bluff-body base is estimated to be of the order of 100 and 1000 respectively for the two TI cases suggesting a substantial difference in their combustion regimes. Laser Doppler Velocimetry (LDV), CARS (Coherent Anti-strokes Raman Spectroscopy), spontaneous Raman scattering, and Rayleigh techniques were employed to measure velocity temperature and species variations inside the combustor and these measurements are used to validate the LES results.

3. LES

The conservation equations for Favre-filtered mass, momentum and energy (total enthalpy) are solved along with two additional equations for combustion modelling. These equations and their numerical treatment are described in this section. The sub-grid stresses, thus the sub-grid viscosity, are modelled using a localised dynamic Smagorinsky model [36,37].

3.1. Combustion models

The thermochemical state of reactant mixture is described using a reaction progress variable, c, in flamelet approach. The progress variable can be defined using temperature or an appropriate species mass fraction and the definition used for this study is given in Section 3.2. A transport equation for its Favre-filtered value, $\widetilde{c}$, is [38]

$$\overline{\rho}\frac{D\widetilde{c}}{Dt} = \nabla\cdot\left[\left(\overline{\rho\mathcal{D}} + \overline{\rho}\frac{\nu_t}{Sc_t}\right)\nabla\widetilde{c}\right] + \overline{\dot{\omega}}. \tag{1}$$

in standard notations with $\mathcal{D}$ as the molecular diffusivity of c. The eddy viscosity, ν_t, and the Schmidt number, Sc_t, are obtained using dynamic procedures as noted above.

The filtered reaction rate, $\overline{\dot{\omega}}$, is modelled using

$$\overline{\dot{\omega}} = \overline{\rho}\int_0^1 \frac{\dot{\omega}(\zeta)}{\rho}\,\widetilde{P}(\zeta;\,\widetilde{c},\sigma^2_{c,\mathrm{sgs}})\;\;\mathrm{d}\zeta\,, \tag{2}$$

where ζ is the sample space variable for c, $\widetilde{P}(\zeta;\,\widetilde{c},\sigma^2_{c,\mathrm{sgs}})$ is the marginal density weighted (Favre) subgrid probability density function (PDF) of c, $\dot{\omega}(\zeta)$ is the flamelet reaction rate, and ρ is the flamelet mixture density. The filtered density obtained in LES is $\overline{\rho}$. A Beta function is used to prescribe the shape of this subgrid PDF for given values of $\widetilde{c}$ and SGS variance, $\sigma^2_{c,\mathrm{sgs}}$, which are obtained by solving their respective transport equations. The integral in Eq. (2) will give numerical difficulties when the PDF is close to bimodal (large $\sigma^2_{c,\mathrm{sgs}}$), which is avoided by using integration by parts technique. This involves the CDF (cumulative distribution function), $\mathcal{C}$, rather than the PDF as detailed in [6]. Briefly, Eq. (2) can be written for a generic quantity Q as

$$\begin{aligned}\overline{Q} &= \int_0^1 Q(\zeta)P(\zeta)\mathrm{d}\zeta = \int_0^1 Q\;\;\mathrm{d}(\mathcal{C})\\ &= Q(\zeta=1) - \int_0^1 \mathcal{C}\,Q'\;\;\mathrm{d}\zeta\,.\end{aligned} \tag{3}$$

The derivative $Q' = \partial Q/\partial\zeta$ is usually well behaved in the domain $0 \le \zeta \le 1$ and thus the integral in Eq. (3) can be evaluated accurately.

The transport equation for the SGS variance is

$$\begin{aligned}\overline{\rho}\frac{D\sigma^2_{c,\mathrm{sgs}}}{Dt} \approx\; &\nabla\cdot\left[\left(\overline{\rho\mathcal{D}} + \overline{\rho}\frac{\nu_t}{Sc_t}\right)\nabla\sigma^2_{c,\mathrm{sgs}}\right] + 2\left(\overline{\dot{\omega}c} - \overline{\dot{\omega}}\widetilde{c}\right)\\ &- 2\,\overline{\rho}\,\widetilde{\varepsilon}_c + 2\,\overline{\rho}\,\frac{\nu_t}{Sc_t}(\nabla\widetilde{c}\cdot\nabla\widetilde{c})\end{aligned} \tag{4}$$

This equation is derived using the transport equations for $\widetilde{c^2}$ and $\widetilde{c}^2$ because $\sigma^2_{c,\mathrm{sgs}} = \widetilde{c^2} - \widetilde{c}^2$. The third and fourth terms of Eq. (4) need closures and the reaction related term is closed using

$$\overline{\dot{\omega}c} = \overline{\rho}\int_0^1 \left(\frac{\dot{\omega}\,\zeta}{\rho}\right)\widetilde{P}(\zeta)\;\;\mathrm{d}\zeta\,, \tag{5}$$

which is consistent with Eq. (2). This integral is evaluated using integration by parts technique noted in Eq. (3) with the required derivative obtained numerically. It is worth noting that the second term in the RHS of Eq. (4) may lead to non-positivity or unboundedness when the integrals in Eqs. (2) and (5) are inaccurate. This is not observed in this study because of the use of integration by parts technique as noted earlier.

The sub-grid dissipation rate is $\overline{\rho}\,\widetilde{\varepsilon}_c = [\overline{\rho\mathcal{D}(\nabla c\cdot\nabla c)} - \overline{\rho\mathcal{D}}(\nabla\widetilde{c}\cdot\nabla\widetilde{c})]$ and is modelled using the algebraic closure investigated in [39]. This closure used in earlier studies [6,40] is

$$\begin{aligned}\widetilde{\varepsilon}_c = &\left[1-\exp\left(-0.75\Delta^+\right)\right]\\ &\times\left[2K_c\frac{s_L}{\delta_{\mathrm{th}}} + (C_3 - \tau C_4\mathrm{Da}_\Delta)\left(\frac{2\,u'_\Delta}{3\Delta}\right)\right]\frac{\sigma^2_{c,\mathrm{sgs}}}{\beta_c}\end{aligned} \tag{6}$$

with $\Delta^+ = \Delta/\delta_{\mathrm{th}}$ as the normalised filter width. The SGS velocity scale is u'_Δ, $s_L = 12.2$ cm/s is the unstrained planar laminar flame speed with a thermal thickness of $\delta_{th} = (T_{ad}-T_u)/|\nabla T|_{\max} = 0.93$ mm, where T_{ad} and T_u are the adiabatic flame and reactant temperatures respectively. The heat release parameter is $\tau = (T_{ad}-T_u)/T_u = 4.56$ for the methane–air mixture used in the experiments. The thermochemical parameter K_c is 0.79τ [39]. The parameters C_3 and C_4 are related to SGS Karlovitz number, $\mathrm{Ka}_\Delta = (u'_\Delta/s_L)^{3/2}(\delta_{th}/\Delta)^{1/2}$, and they are given by $C_3 = 1.5\sqrt{\mathrm{Ka}_\Delta}/(1+\sqrt{\mathrm{Ka}_\Delta})$ and $C_4 = 1.1/(1+\mathrm{Ka}_\Delta)^{0.4}$ [39]. The SGS Damköhler number is $\mathrm{Da}_\Delta = t_{\mathrm{sgs}}/t_c$ where $t_c = \delta_{th}/s_L$ is the chemical time scale and $t_{\mathrm{sgs}} = k_{\mathrm{sgs}}/\epsilon_{\mathrm{sgs}}$ is the SGS flow time scale which is related to u'_Δ and Δ. The symbols $k_{\mathrm{sgs}} \approx 3\,u'^2_\Delta/2$ and $\epsilon_{\mathrm{sgs}} \approx u'^3_\Delta/\Delta$ are the SGS kinetic energy and its dissipation rate.

Following earlier studies [6,40], the SGS velocity scale u'_Δ is estimated using scale-similarity [41], $u'_\Delta = \sum_i |\widetilde{u}_i - \widehat{\widetilde{u}}_i|$, where $\widehat{\cdot}$ refers to test filtering operation. The only adjustable parameter in Eq. (6) is β_c which is computed using dynamic approach described in [40,42]. Thus, this dissipation rate model does not have a tunable parameter for this study.

The subgrid variance can also be prescribed using a common algebraic model $\sigma^2_{c,\mathrm{sgs,mod}} \approx \mathcal{A}\Delta^2(\nabla\widetilde{c}\cdot\nabla\widetilde{c})$, where $\mathcal{A}$ is a model parameter of order unity. This model was shown [6] to be inappropriate for premixed combustion and is also studied here by comparing $\sigma^2_{c,\mathrm{sgs,mod}}$ to $\sigma^2_{c,\mathrm{sgs}}$ in Section 4.2.

3.2. Numerical procedure

The simulations are conducted using PRECISE-MB [43], which is based on finite volume method for low-Mach reacting flow equations. The Favre-filtered momentum equation is solved first followed by the continuity equation for pressure correction through SIMPLEC algorithm [44].

The transport equation for Favre-filtered total enthalpy, $\widetilde{h}$,

$$\overline{\rho}\frac{D\widetilde{h}}{Dt} = \frac{\partial}{\partial x_j}\left(\overline{\rho\,\alpha\frac{\partial h}{\partial x_j}}\right) - \frac{\partial\left(\overline{\rho u_i h} - \overline{\rho}\,\widetilde{u}_i\,\widetilde{h}\right)}{\partial x_i} \tag{7}$$

is included to track the mixing of reactant and air streams enthalpies at the combustor exit, see Fig. 1b, and the requirement to include the air stream for the calculation is discussed in Section 3.3. The turbulent transport term in this and other scalar transport equations is modelled using a gradient hypothesis and dynamic Schmidt number approach [37].

The temperature is obtained using $\widetilde{T} = T_0 + (\widetilde{h} - \widetilde{\Delta h}^0_{f,\mathrm{mix}})/\widetilde{C}_{p,\mathrm{mix}}$, where $T_0 = 298.5$ K is the reference temperature. The formation enthalpy and specific heat capacity at constant pressure of the gas mixture are $\widetilde{\Delta h}^0_{f,\mathrm{mix}}$ and $\widetilde{C}_{p,\mathrm{mix}}$, respectively, and this specific heat capacity is temperature dependent as described in [45]. The mixture density is computed using the state equation, $\overline{\rho} = \overline{p}\widetilde{W}_{\mathrm{mix}}/(R_0\widetilde{T})$, where $\overline{p}$ is the pressure, $\widetilde{W}_{\mathrm{mix}}$ is the mixture molecular weight and R_0 is the universal gas constant. The values for $\widetilde{\Delta h}^0_{f,\mathrm{mix}}$, $\widetilde{C}_{p,\mathrm{mix}}$ and $\widetilde{W}_{\mathrm{mix}}$ are obtained from flamelet solution using equations similar to Eq. (2). These values tabulated as a function of $\widetilde{c}$ and $\sigma^2_{c,\mathrm{sgs}}$ are used for LES. The flamelet (unstrained planar laminar flame) is computed using PREMIX code [46] and GRI 3.0 chemical kinetic mechanism for methane–air combustion,

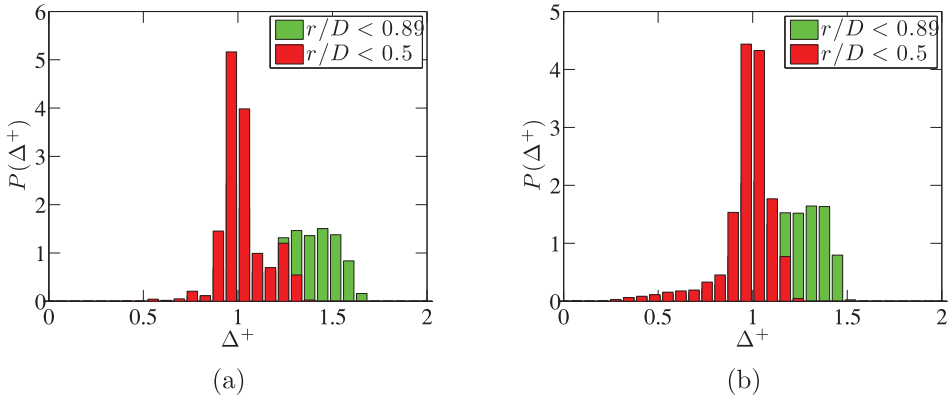

Fig. 2. Histogram of $\Delta^+ = \Delta/\delta_{th}$ for (a) 1.8M and (b) 2.2M grids are shown for the entire combustor volume (green) and a smaller part of it (red). (For interpretation of the references to colour in this figure legend, the reader is referred to the web version of this article).

and the values for s_L, δ_{th} and τ obtained from this calculation are used in Eq. (6). The progress variable is defined as

$$c = 1 - \frac{Y_{\text{CH4}}}{Y^u_{\text{CH4}}}, \tag{8}$$

where $Y^u_{\text{CH}_4}$ is the methane mass fraction in the reactant mixture. The sensitivity of results to c definition is explored in Section 4.5.

3.3. Computational domain, grid and boundary conditions

The computational domain began at 58 mm upstream of the bluff-body base as shown in Fig. 1b and this boundary was specified as the inlet using measured reactant mass flow rate. The intricate geometry of the turbulence generating device used in the experiments was excluded. However, turbulence at this inlet was specified using digital filter technique [47] and its level was adjusted to get TI of about 24% at the combustor entry (base of the bluff-body, see Fig. 1) as in the experiments. There was no turbulence grid for the 2% case in the experiment and thus no synthetic turbulence was specified for the simulation of this case. An additional domain of $4.5D \times 4.5D \times 17.5D (= 778\,\text{mm})$ was added at the combustor exit as in Fig. 1b to avoid numerical waves reflected by the exit if this additional domain was absent. This treatment improved the numerical stability of the simulations. The no-slip combustor walls were specified to be adiabatic whereas the walls of the additional domain were treated to be slip walls. All variables were specified to have zero gradients at the computational domain outlet. It is worth noting that heat losses were observed to be small in the experiments [16] and thus it is reasonable to treat the walls as adiabatic.

Since the boundary layer is not expected to be fully developed behind the turbulent generator, a flat velocity profile with $U_0 = 11.5\,\text{m/s}$ was specified at the inlet boundary based on the measured mass flow rate and this gave $U_{\text{ref}} = 15\,\text{m/s}$ at the combustion chamber entrance (see Fig. 1a). A small velocity of $U_{\text{air}} = 0.2\,\text{m/s}$ was specified as illustrated in Fig. 1b for the additional computational domain to mimic the air entrainment at the burner exit. The computational domain was discretised using two block-structured meshes having 1.8 and 2.2 M cells in total and these two grids had about 47 cells for D. The main difference between these two grids was in the near-wall resolution used for the bluff-body boundary layers.

The wall refinement can be characterised using dimensionless wall distance, $y^+ = yu^*/\nu$, where y is the local distance normal to the wall, ν is the kinematic viscosity and u^* is the friction velocity defined as $u^* = \sqrt{\tau_w/\rho}$ with τ_w as the wall shear stress. The dimensionless wall distance estimated from the experimental data [18,19] was used to guide the grid distribution. Approximately 2 cells were placed in the viscous sublayer ($y^+ \leq 5$) for 2.2 M grid and the near-wall cell size was $y^+ \approx 9$ on the sides of bluff body and 90 on its base for the 1.8 M grid. The larger y^+ was used for the bluff body base because the recirculation zone was expected to reduce the velocity gradients there. Since the first cell was outside the viscous sub-layer, the wall functions were employed for simulations using the 1.8 M grid.

A representative filter size may be calculated as the cube root of numerical cell volume and histogram of this filter width, normalised using δ_{th}, is shown in Fig. 2 for both grids. This histogram illustrates the cell size distribution in the entire combustor volume, $0 \leq x \leq 6D$ with $r \leq 0.89\,D$, and in a smaller part, $r \leq 0.5\,D$, for the two grids. The peak is at $\Delta^+ \approx 1$ for both grids and there is a long tail with $\Delta^+ < 1$ for the 2.2 M grid. Although these grids are relatively small compared to what is commonly used for LES of combusting flows, they are adequate to yield accurate results for the modelling framework used here as one shall see in the next section.

The simulations were run using 80 cores of Darwin cluster at Cambridge University for a period of ten flow-through times and this took about 12 h on a wall clock for 2.2 M grid. The flow-through time, τ_f, was defined as twice the length of the combustor divided by U_{ref}. The samples were collected for $6\tau_f$ after allowing $4\tau_f$ for initial transients to escape the computational volume and this time was observed to be sufficient to reach a stationary state in the recirculation zone and in other parts of the computational domain for the combustor. The 6 flow-through time corresponds to a physical time of 0.18 s. The time step for simulations was set to have a maximum CFL (Courant–Friedrichs–Lewy) number of 0.3 in the entire computational domain.

4. Results and discussion

4.1. Cold flow

Non-reacting flow was simulated first to assess the computational model and characteristics such as recirculation zone size are used for this assessment. Figure 3 compares the computed and measured normalised mean axial velocity, $\langle U \rangle / U_{\text{ref}}$, along the centreline for the 2% and 24% TI cases. No synthetic turbulence was specified at the inlet for the 2% case since there was no turbulence grid present in the experiment [17]. The recirculation zone length, L_r, is underestimated in the 1.8 M grid and the amount of this under-estimation is independent of near-wall treatment as seen in Fig. 3. The computed recirculation zone length for 2.2 M grid agrees well with the measured value for both TI cases. Since there was no full experimental characterisation of the turbulence, its level at the computational domain inlet was adjusted, by about

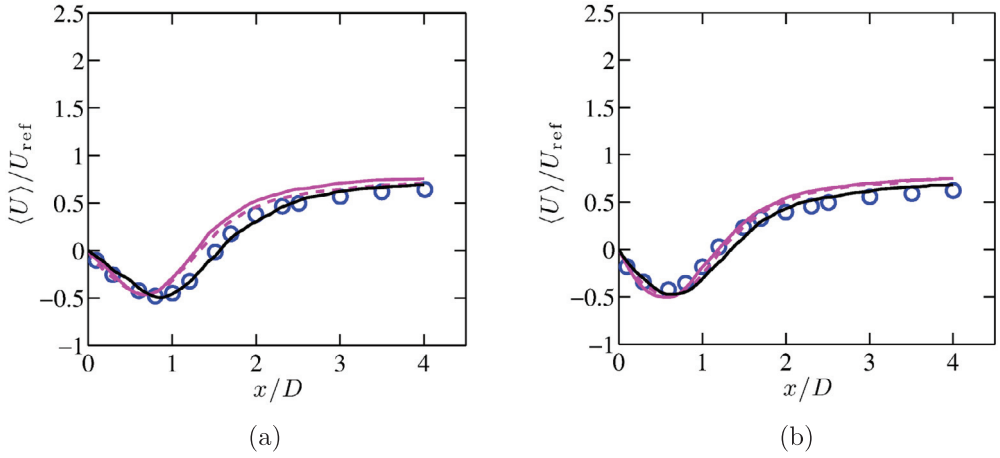

Fig. 3. Centreline variation of computed (lines) and measured [17] (symbols) $\langle U \rangle / U_{\mathrm{ref}}$ in cold flow with (a) 2% and (b) 24% TI. The results are shown for both 1.8 M (——) and 2.2 M (——) grids. The result obtained using wall function is shown only for 1.8 M grid (– –).

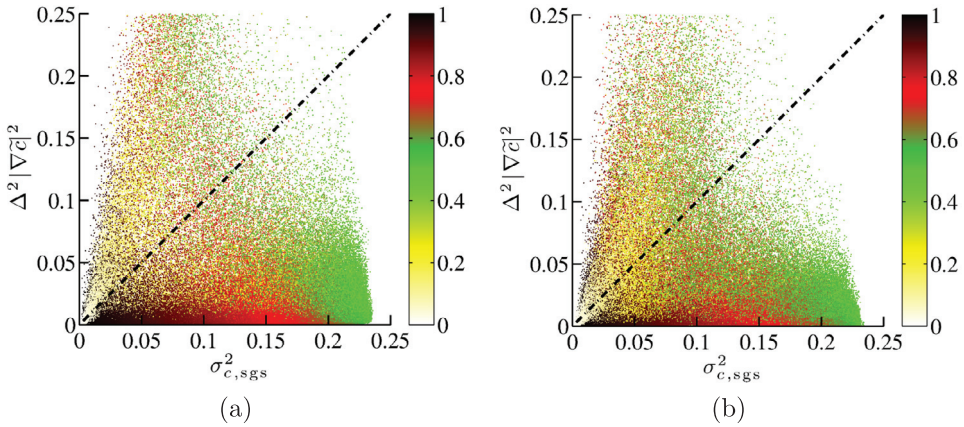

Fig. 4. Comparison of $\sigma^2_{c,\mathrm{sgs}}$ and $\sigma^2_{c,\mathrm{sgs,mod}}$ for (a) 2% and (b) 24% TI cases at an arbitrary time. Colours represent filtered progress variable, $\widetilde{c}$, values. (For interpretation of the references to colour in this figure legend, the reader is referred to the web version of this article).

3%, for the results shown in Fig. 3. Overall, the comparison shown in this figure confirms that the grid and numerical conditions used to simulate the burner flow and its attributes are excellent. Based on these results, the reacting flow results discussed in the following sections are shown for the 2.2 M grid without the wall functions. The 1.8 M grid results with the wall functions will be shown only for comparison purposes when specified.

4.2. Combusting flow

The experimental study [16] divided the combusting flow into three regions, viz., (i) flamelet region, $0 \leq x/L_r \leq 0.12$, where the flame was thin with combustion time scale was shorter than turbulence time scale; (ii) thin reaction zone region, $0.12 < x/L_r < 1$, where the flame was thickened by coherent structures and the combustion in this region was identified to be in the thin reaction zones regime of turbulent premixed combustion; and (iii) distributed combustion region, located further downstream of the rear stagnation point, where turbulent eddies distribute the flamelets over a broader region and influence at least the preheat layer structure. This definition is different from the classical viewpoint for this combustion regime. Since the turbulence level is large near the bluff-body base and decays in the downstream region the Damköhler number increases with downstream distance suggesting that the combustion condition moves from distributed to flamelet regime as was shown experimentally in [19]. The three regions discussed above are marked in Figs. 7 and 12 as R1, R2 and R3 respectively for visualisation purpose, and these figures are to be discussed later. It is unclear how well the flamelet assumption holds in these regions because of the different combustion regimes. This is assessed by comparing measurements and LES statistics. The experimental data are available for the first two regions in both, 2% and 24%, TI cases but the measurements in the third region are available only for the 24% TI case.

Before discussing these results in detail, it is worth to make some remarks on the modelling of SGS variance. It is quite common to use an algebraic model, $\sigma^2_{c,\mathrm{sgs,mod}} \approx \mathcal{A}\Delta^2(\nabla\widetilde{c}\cdot\nabla\widetilde{c})$, where $\mathcal{A}$ is the model parameter, for the SGS variance. Typical value for $\mathcal{A}$ is about 0.5 and if one uses a dynamic procedure then it has some variations over this value. This model was derived for a passive scalar by balancing the dissipation and turbulent production of the variance, the last two terms of Eq. (4), ignoring contributions from the reaction rate, the third term in that equation. The order of magnitude analysis in [6] showed that the reaction term cannot be ignored and indeed the variance transport equation must be solved. In the light of this analysis, it is useful to compare $\sigma^2_{c,\mathrm{sgs,mod}}$ with $\sigma^2_{c,\mathrm{sgs}}$ obtained using Eq. (4). This comparison is shown in Fig. 4 for both TI cases at an arbitrary time and $\mathcal{A}$ is taken to be 1 for simplicity. If the two variances are similar then the data would lie around the diagonal line, but the scatter observed in the figure suggests that the algebraic model overestimates the variance for $\widetilde{c} \leq 0.4$ and it underestimates for $\widetilde{c} > 0.4$ in comparison to those

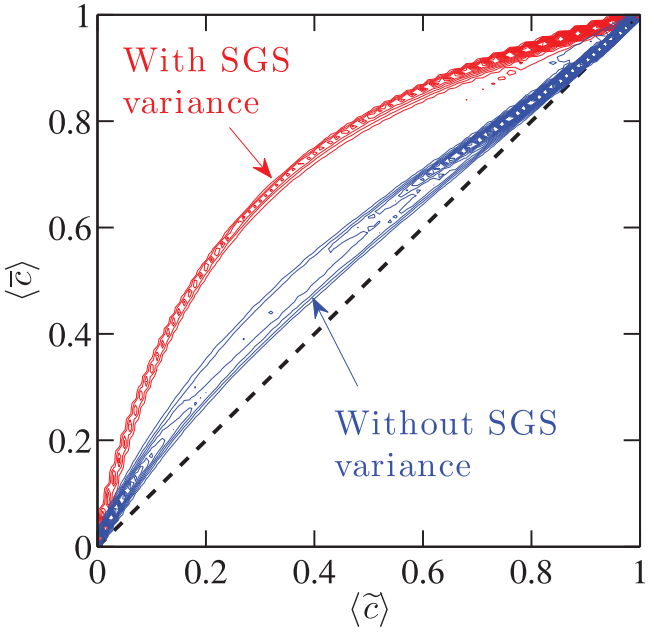

Fig. 5. Contours of 2D histogram of time-averaged progress variables, $\langle \widetilde{c} \rangle$ and $\langle \overline{c} \rangle$ for the 24% TI case.

obtained using the transport equation. A similar behaviour was reported for piloted [6] and non-piloted [48] Bunsen flames. However, one must be careful in drawing any conclusion from this result because LES data is used and it is more appropriate to use direct numerical simulation (DNS) data for this type of analysis. Nevertheless, based on the order of magnitude analysis presented in [6] one may expect a similar behaviour for the algebraic model even with the DNS data because it ignores the reaction rate contribution. Hence, the SGS variance computed using its transport equation is used for further analysis presented below.

The species mass fractions and temperature were measured using CARS and spontaneous Raman scattering techniques in the experimental investigations [16–19] and these were suggested [16] to be the Reynolds-averaged values. The LES statistics are Favre-averaged and hence one must convert this into Reynolds-averaged values (indicated by an over-bar below) and this is achieved using [49]

$$\langle \overline{T}^{+} \rangle = \langle \widetilde{T}^{+} \rangle + \tau \frac{\sigma^2_{T^+}}{1 + \tau \langle \widetilde{T}^{+} \rangle} \tag{9}$$

where $\langle \widetilde{T}^{+} \rangle = \left(\langle \widetilde{T} \rangle - T_0 \right) / (T_{ad} - T_0)$ is the normalised Favre-averaged temperature. The total variance $\sigma^2_{T^+}$ is the sum of resolved and SGS variances:

$$\sigma^2_{T^+} = \sigma^2_{T^+,\mathrm{res}} + \langle \sigma^2_{T^+,\mathrm{sgs}} \rangle. \tag{10}$$

Since the Lewis number for the reactant mixture used is close to unity the mean SGS part is approximated as $\langle \sigma^2_{T^+,\mathrm{sgs}} \rangle \approx \langle \sigma^2_{c,\mathrm{sgs}} \rangle$. The resolved part is $\sigma^2_{T^+,\mathrm{res}} = \langle \widetilde{T}^{+2} - \langle \widetilde{T}^{+} \rangle^2 \rangle$.

Equations similar to Eqs. (9) and (10) can be written for $\widetilde{c}$ [49] and hence the Favre- and Reynolds-averaged progress variable can be compared. The influence of $\langle \sigma^2_{c,\mathrm{sgs}} \rangle$ can be understood by calculating $\langle \overline{c} \rangle$ with and without this variance. The results are shown in Fig. 5 for the 24% TI case as contours of joint normalised histogram of Favre-averaged, $\langle \widetilde{c} \rangle$, and Reynolds-averaged, $\langle \overline{c} \rangle$, progress variable fields in the entire combustor. The contours will follow the diagonal line shown if $\tau = 0$ or $\sigma^2_c = 0$, which is not the case for turbulent combustion. Note that the total variance is the sum of resolved and SGS variances as in Eq. (10). Figure 5 shows that the contours move far from the diagonal line when the SGS variance is included in the calculation of $\langle \overline{c} \rangle$ showing that $\langle \sigma^2_{c,\mathrm{sgs}} \rangle$ contribution is large. This is because combustion is a SGS phenomenon playing a central role in the generation of sub-grid fluctuation of c. Hence, the contribution of the SGS variance cannot be ignored and due care is required while comparing LES statistics with measurements.

Typical variation of the ratio between the averaged resolved and SGS variances, $\sigma^2_{c,\mathrm{res}} / \langle \sigma^2_{c,\mathrm{sgs}} \rangle$, with $\langle \widetilde{c} \rangle$ shown in Fig. 6a for the 24% TI case suggests that the SGS variance is nearly 2–3 times larger than the resolved part for most part of the flame brush. Values larger than 0.75 are rare and they occur in the mixing layer between the burning mixture and cold reactant, and hence for low values of $\langle \widetilde{c} \rangle$ as seen in Fig. 6a. The total variance, σ^2_c, at various streamwise locations shown in Fig. 6b follows the typical quadratic variation with $\langle \widetilde{c} \rangle$. The maximum possible value of $\langle \widetilde{c} \rangle (1 - \langle \widetilde{c} \rangle)$, is also shown using a dashed line for comparison. This maximum value would be obtained in the limit of very large Damköhler number (BML limit) [50,51]. Thus, the results suggest that the combustion is flamelet-like in the region up to $x \leq 3D$ (almost maximum variance with small scatter) and the combustion is likely to be of distributed reactions (as intended in the beginning of this section) for other downstream locations (smaller variance with large scatter). There may be just mixing without reactions inside the recirculation zone and thus the variance can increase moving downstream for $x \leq 3D$. These observations agree with the experimental observations in [16,19]. The variations in the 2% TI case are very similar to that shown in Fig. 6.

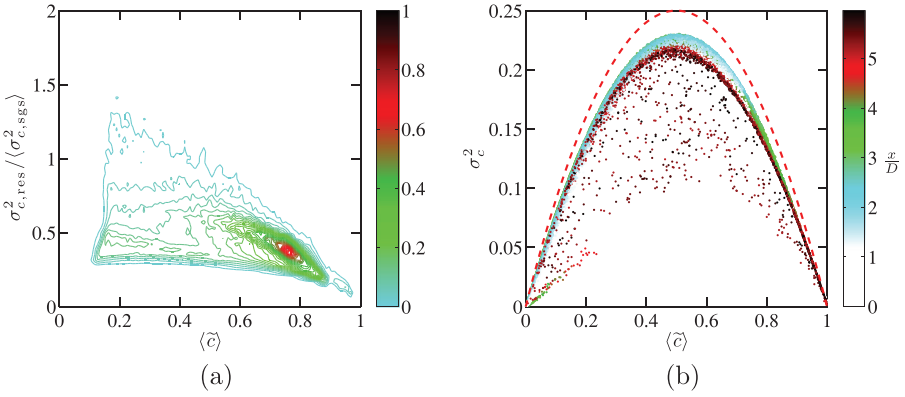

Fig. 6. (a) Contours of normalised histogram of the ratio between time-averaged resolved and SGS variances, $\sigma^2_{c,\mathrm{res}} / \langle \sigma^2_{c,\mathrm{sgs}} \rangle$, versus Favre-averaged progress variable, $\langle \widetilde{c} \rangle$, and (b) scatter plot of total variance, $\sigma^2_c = \sigma^2_{c,\mathrm{res}} + \langle \sigma^2_{c,\mathrm{sgs}} \rangle$, versus $\langle \widetilde{c} \rangle$ at various axial locations for 24% TI case. Colours indicate histogram values in (a) and normalised axial position, x/D, in (b). (For interpretation of the references to colour in this figure legend, the reader is referred to the web version of this article).

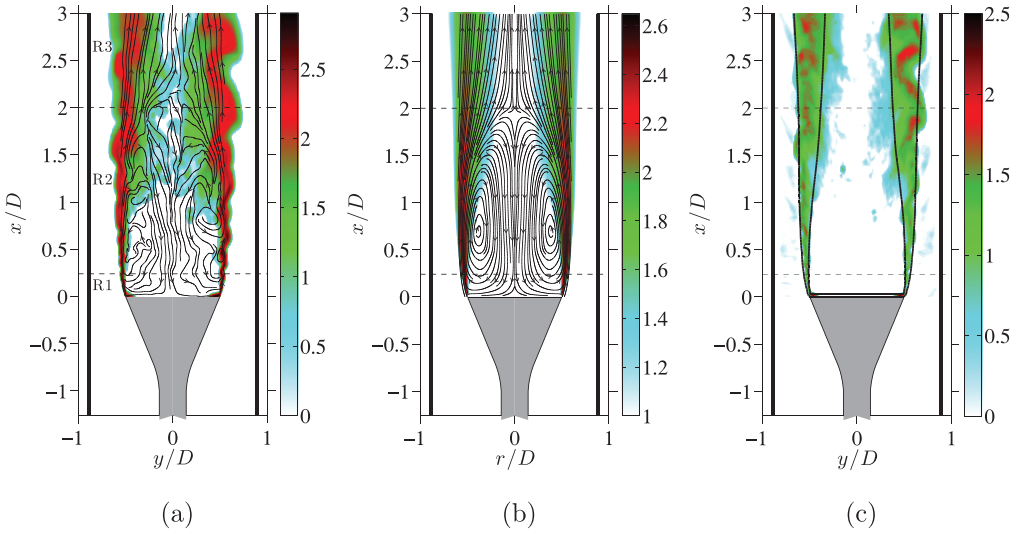

Fig. 7. Stream lines of (a) filtered and (b) averaged velocity fields along with the corresponding reaction rate contours (in colours) for the 2% TI case in the mid-plane. The reaction rates are shown as $\log(1000\overline{\dot{\omega}}^{+})$, where $\overline{\dot{\omega}}^{+} = \overline{\dot{\omega}}\delta_{th}/(\rho_u s_L)$. The contours of $\log(1000\,\widehat{\mathrm{Da}}_{\Delta})$ is shown in colours in (c) along with $\langle\widetilde{c}\rangle = 0.1$ and 0.9 iso-lines. (For interpretation of the references to colour in this figure legend, the reader is referred to the web version of this article).

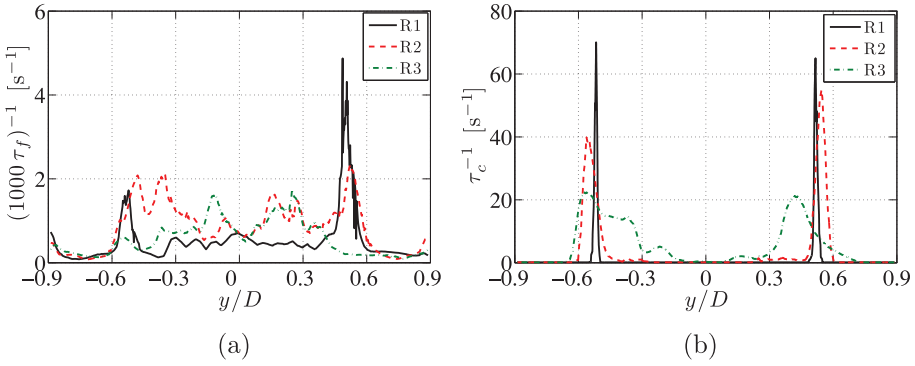

Fig. 8. Typical variations of inverse of SGS (a) turbulent timescale and (b) chemical timescale with y/D for the results shown in Fig. 7a.

4.2.1. 2% approach turbulence case

Pan et al. [16] observed that the flame (also the flame brush) was thin near the base and the flame brush became thicker as one moved downstream. The flame brush at $x \approx 2D$ (the rear stagnation point), was noted in this experimental study to be almost 12 times thicker compared to that near the base. The flame brush thickness was estimated using the radial gradient of averaged temperature in [16] and the same approach was employed for LES. Similar variations are observed in Fig. 7 showing the variations of filtered and averaged reaction rates, and local SGS Damköhler number $\widehat{\mathrm{Da}}_{\Delta} = \overline{\dot{\omega}}\,\Delta/\left(\rho_u\, u'_{\Delta}\right)$, in the computational domain mid-plane. The contours of $\langle\widetilde{c}\rangle = 0.1$ and 0.9 are also shown in Fig. 7c to denote the flame brush. Just to remind ourselves, the three regions observed in the experimental study [16] (see Section 4.2) are marked as R1–R3 in Fig. 7. The filtered reaction zone is very thin close to the bluff-body but its width increases as one moves downstream. This behaviour is also seen for the averaged reaction rate and the width of this zone does not seem to increase much for $x \geq 2D$ which is quite clear with the contours of $\langle\widetilde{c}\rangle$. The reaction zone structure in this region is likely to be influenced by turbulence and the finite rate chemistry effects become non-negligible. These effects appear through patches of high and low filtered reaction rate. This is clearer in Fig. 7c showing $\widehat{\mathrm{Da}}_{\Delta}$ which is the ratio between SGS turbulent and combustion time scales and thus it is easy to see the relative importance of these two scales in different regions of the combustor. Typical variations of inverse of SGS turbulent timescale, $\tau_f = \left(\Delta/u'_{\Delta}\right)$, and chemical timescale, $\tau_c = \left(\rho/\overline{\dot{\omega}}\right)$, with y/D are shown in Fig. 8. The Damköhler number (see Fig. 7c) is related to these two timescales through $\widehat{\mathrm{Da}}_{\Delta} = \tau_f/\tau_c$. These curves in Fig. 8 are 1D cuts of the results given in Fig. 7 and are shown for three locations $x/D = 0.15$, 1.0 and 2.5. These locations are respectively in the regions R1, R2 and R3. Since the results in Fig. 8 are for specific locations, typical ranges for these quantities are given in Table 1.

Table 1
Typical ranges of $f = \log(1000\,\overline{\dot{\omega}}^{+})$, $d = \log(1000\,\widehat{\mathrm{Da}}_{\Delta})$, τ_c and τ_f in the three regions.

Region	f	d	τ_c(ms)	τ_f(ms)
R1	2.3–3	0.3–1.2	7.6–38.2	0.08–0.12
R2	2.2–2.7	0.9–1.8	15.2–48.1	0.38–0.95
R3	1.9–2.3	1.4–2.0	38.2–96.0	2.4–3.8

Relatively low values of $\widehat{\mathrm{Da}}_{\Delta}$ near the edges of bluff-body are probably due to high level of mixing and low chemical activity which is consistent to the experimental observations [16,19], but could also be due to some intermittency in the axial velocity fluctuation as the flame in this region is expected to be quasi-laminar. The value of $\widehat{\mathrm{Da}}_{\Delta} \sim 0.01$ is because of spatio-temporal intermittency effects and a value for $\widehat{\mathrm{Da}}_{\Delta}$ of order unity is not observed in regions of flame suggesting that the SGS fluid dynamic

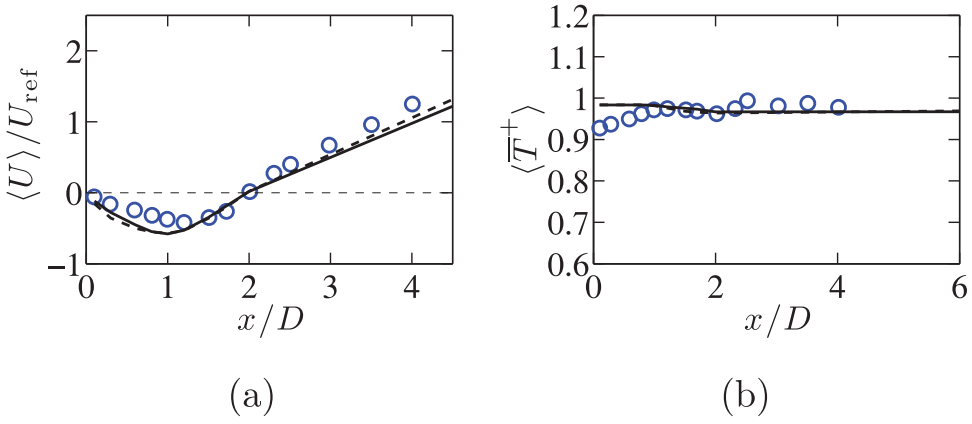

Fig. 9. Centreline variation of (a) $\langle U\rangle/U_{\rm ref}$ and (b) $\langle T^+\rangle$ in 2% TI case for 1.8 M (– –) and 2.2 M (——) grids. Experimental data [16,17] are shown as symbols.

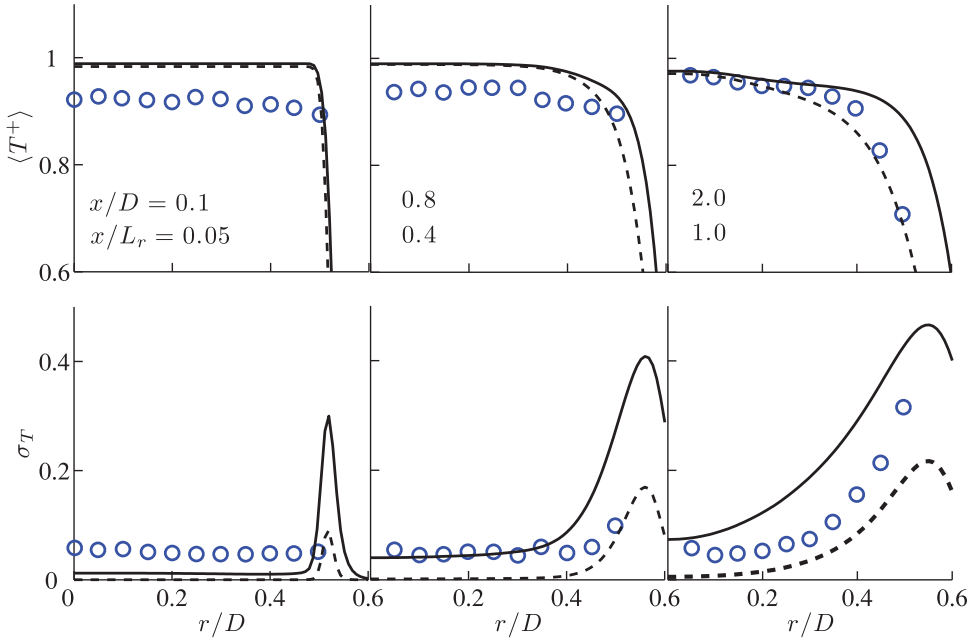

Fig. 10. Radial variations of $\langle \widetilde{T}^+\rangle$ (– –) and $\langle \overline{T}^+\rangle$ (——) for 2.2 M grids are compared with experimental data [16,17] (symbols). The resolved (dashed line) and total (solid line) rms values are compared to the measurement in the bottom row.

time scale is typically shorter than the chemical timescale as noted in Table 1. This suggests that the finite rate chemistry effects are important in these flames, which must be noted while comparing the LES statistics with measurements. The $\widehat{\rm Da}_\Delta$ increases downstream because turbulence decays and the combustion is almost complete (see Table 1).

Figure 9a compares the centreline variation of measured [17] and computed averaged axial velocity, $\langle U\rangle$, normalised using $U_{\rm ref}$ (see Fig. 1). The adiabatic condition imposed on the bluff-body caused the flow to accelerate more leading to the underestimate of $\langle U\rangle$ for $x < D$. However, the computed recirculation zone length, $L_r \approx 2D$, agrees well with the measured value. The centreline variation of computed and measured normalised mean temperature is compared in Fig. 9b and this comparison is very good apart for some small overestimates resulting from the adiabatic condition used for the bluff-body. Overall, the predictions are good and the grid sensitivity is small.

The radial variations of $\langle \widetilde{T}^+\rangle$ and $\langle \overline{T}^+\rangle$, obtained using Eq. (9), are compared to measurements in Fig. 10 for three axial locations. The burnt mixture temperature is over predicted by about 6–8% and this over prediction decreases as one moves from $x/D = 0.1$–2. It is also worth to recall that the combustion is flamelet like for $x/D \leq 4.5$ from Fig. 6b and thus the over prediction in temperature is because of the adiabatic condition used for the bluff-body in the simulation. This over prediction is consistent with about 5–8% heat losses observed in experiments [16]. The temperature variation inside the flame brush is predicted quite well and also the influence of density weighting is seen for the flame brush region, which is consistent with the results in Fig. 5. The normalised temperature rms increases inside the flame brush because of combustion effects which is quite strong for $x = 2D$ location and this trend is predicted well in the computations. The resolved rms, $\sigma_{T^+,\rm res}$, is quite close to the experimental data, but including the SGS contribution of $\langle \sigma_{T^+,\rm sgs}\rangle \approx \langle \sigma_{c,\rm sgs}\rangle$ results in a large over prediction although the trend is captured. The above approximation for $\sigma_{T^+,\rm sgs}$ seems to overestimate this contribution and one may have to transport it. However, the comparison shown in this figure is satisfactory.

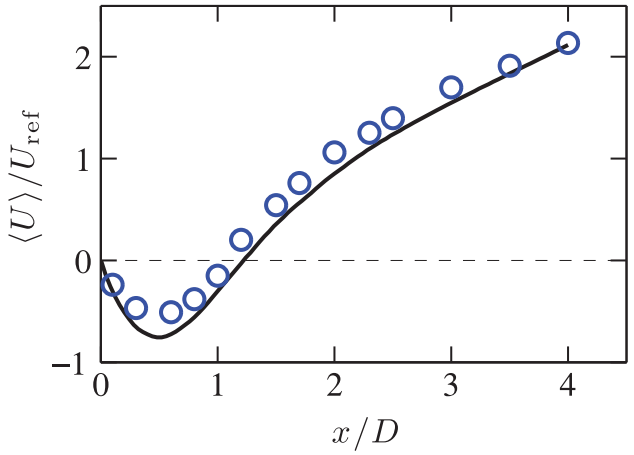

Fig. 11. Centreline variation of computed (lines) and measured [16,17] (symbols) $\langle U \rangle / U_{\rm ref}$ for 24% TI case.

4.2.2. 24% approach turbulence case

An increase in the turbulence level at the inlet will change the flow and combustion characteristics behind the bluff-body. The recirculation zone length was observed to decrease from 2*D* to 1.3*D* when the incoming turbulence intensity was increased from 2% to 17% and increasing the turbulence level further by 5% resulted in a recirculation zone length of 1.1*D*, i.e., the length decreased by about 15% [16,17]. This high sensitivity to the incoming turbulence and a lack of its full characterisation in the experiments pose challenges for simulations. Despite this, an attempt is made here to simulate the 24% TI case (as referred in the experimental studies) because a good set of scalar measurements were reported in [16–19], which are useful for model validation.

The synthetic turbulence level fed at the inlet was varied by about 3% as noted in Section 4.1 to match the cold flow characteristics and this inlet condition was maintained for the reacting flow simulations investigated below. This produced an average TI of about 19% at entry to the combustor, $x = 0$, and gave a reasonable centreline variation of $\langle U \rangle / U_{\rm ref}$ shown in Fig. 11 although there is a small overestimate (~12%) of the recirculation zone length. However, overall estimate of the flame and flow characteristics obtained using the above approach is reasonable as one shall see next.

A. Reaction rates

Typical contours of filtered and time-averaged reaction rate are shown in Fig. 12 on the mid-plane of the computational domain. The reaction rates are normalised using ρ_u, s_L and δ_{th} and are shown in logarithmic scale. The filtered flame is much more wrinkled and corrugated than for the 2% TI case shown in Fig. 7a because of the increased turbulence level. Also, the peak $\overline{\dot{\omega}}^+$ for $x >$ 1.5*D* is reduced significantly compared to those for the upstream locations, which suggests that the combustion is nearly complete in the recirculation zone as was observed in the experiments [18]. The three regions, R1–R3, with combustion occurring in flamelet, thin reaction zones and distributed combustion regimes are also marked in the figure. The typical attributes of these combustion regimes is seen in the filtered reaction rate contours. The reaction rate is confined to a very thin layer in the R1 region and is spread over a thicker flame, represented approximately using $\overline{\dot{\omega}}^+ = 0.1$ contours, but the intense reactions are confined to thin zones in region R2. The later attribute is lost in the R3 region with moderate reactions distributed over the whole width. This agrees with the qualitative description provided in [16]. Streamlines of the mean flow in the right half of Fig. 12 show that the recirculation length is about 1.23 *D*. The flame brush is thin in the R1 region

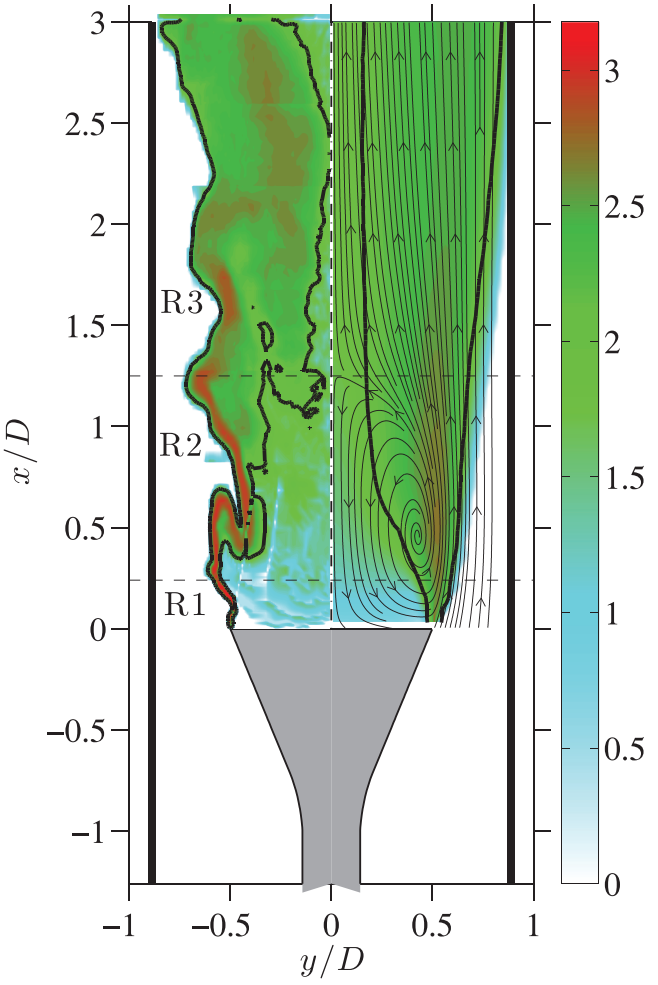

Fig. 12. Contours of $\log(1000\,\overline{\dot{\omega}}^+)$ and $\log(1000\,\langle\overline{\dot{\omega}}^+\rangle)$ for 24% TI case (in colours) in the mid-plane of the computational domain. The reaction rate is normalised using $\rho_u s_L/\delta_{th}$. Isolines having the respective normalised value of 0.1 are shown as bold black lines and the streamlines of averaged flow field are shown in the right half. (For interpretation of the references to colour in this figure legend, the reader is referred to the web version of this article).

and it thickens gradually as one moves downstream. The presence of the three regions is much more distinct for the large TI case compared to the low TI case shown in Fig. 7.

B. Comparison of velocity and temperature statistics

(1) Centreline variations

The centreline variations of $\langle U \rangle / U_{\rm ref}$ was discussed in Fig. 11 and $\langle \overline{T}^+ \rangle$ shown in Fig. 13 is almost constant throughout the combustor, and it is under predicted by a small amount when $\sigma^2_{T^+,\rm sgs}$ is included. The solid line in the figure included only $\sigma^2_{T^+,\rm res}$ and a significant improvement is observed when the SGS variance is included in Eq. (10). An earlier study [22] showing similar underestimate (difference between symbols and solid line in Fig. 13) suggested that this could arise from fluid dynamic strain effects, which is contrary to the expected influence – the strain will not change peak flamelet temperature for unity Lewis number unless its magnitude is so large to cause local extinction, see Fig. 10.3.3 of [52]. Similar influence of the SGS variance is also seen for the radial variation of mean temperature to be discussed next. Hence, the SGS variance plays an important role and its influence should not be ignored for LES of premixed combustion.

(2) Comparison of radial variations

The radial variations of $\langle U \rangle / U_{\rm ref}$ and $\langle V \rangle / U_{\rm ref}$, where *V* is the radial velocity, are shown in Fig. 14 for six axial locations covering

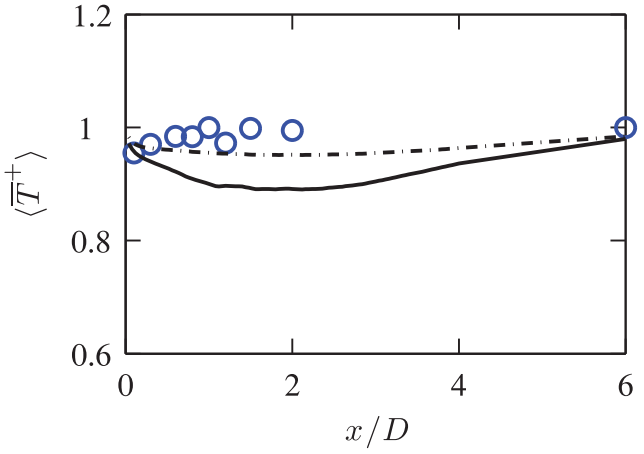

Fig. 13. Centreline variation of computed (lines) and measured [16,17] (symbols) normalised mean temperature. The influence of time-averaged sub-grid variance, $\langle \sigma^2_{\tilde{T}^+,sgs} \rangle$, is shown; solid line – excluding $\langle \sigma^2_{\tilde{T}^+,sgs} \rangle$ contribution and dash-dotted line – including its contribution.

$L_r \approx 1.2D$. As noted earlier, there is a small difference in the measured and computed L_r which leads to the small differences in $\langle U \rangle$ and $\langle V \rangle$ observed for locations $x/D = 1$ and 1.2 in Fig. 14. These results are shown for regions of flamelet combustion marked as R1 and R2 in Fig. 12 and, the corresponding variations of normalised mean temperature and rms are shown in Fig. 15 along with the measurements obtained using Rayleigh [18,19] and CARS [16] techniques. The difference between these two measurements is negligible and the measured rms values were reported only for $x \leq 0.6\,D$. The normalised mean temperature does not vary with the axial position for $r \leq 0.4\,D$ [16] and a similar behaviour is observed for the computed $\langle \overline{T}^+ \rangle$, which also agrees well with the measurements for all the axial locations. The Favre averaged normalised temperature is substantially lower than the measured values, specifically in the flame region, $0.4 \leq r/D \leq 0.7$ and is related to $\langle \overline{T}^+ \rangle$ through Eq. (9). Hence, the total variance of temperature must be calculated with care. The computed radial variation of normalised temperature rms is compared to the experimental data in Fig. 15; the solid line is for the resolved part and the dash-dotted line is for the total rms given by Eq. (10). The agreement is improved when the SGS part is included confirming the importance of $\sigma^2_{\tilde{T}^+,sgs}$. The rms values measured using Rayleigh and CARS techniques do not differ much as seen in Fig. 15. Overall, the comparisons shown in this figure are very good.

4.3. Comparison for post-recirculation region

The filtered flame in this region is thickened by turbulent eddies and the combustion is in the distributed combustion regime [16,17] (see Section 4.2). Figure 16 compares the measured [17] and computed normalised mean velocities for $x/D = 1.5, 1.7$ and 2 locations. A small over prediction of L_r (see Fig. 11) yields some underestimation for the mean axial velocity and the computed radial velocity agrees well with measured values.

The radial variation of normalised time and Favre-averaged temperatures (see Eq. 9) are shown in Fig. 17 along with the measurements [18,19]. The two averages differ substantially in regions with increase in mean temperature. The normalised temperature rms is reported [18,19] only for $x = 6D$ and the comparison shown is good. The peak value is captured well when the SGS contribution is included and there is some overestimation for $0.4 \leq r/D \leq 0.6$. The reason for this is unclear at this time, perhaps one may have to transport $\sigma^2_{\tilde{T}^+,sgs}$ in the simulations rather than taking $\sigma^2_{\tilde{T}^+,sgs} = \sigma^2_{c,sgs}$, which is to be explored in future.

4.4. Comparison of species mass fractions

The measured values of time-averaged species mass fractions were reported for CH_4, O_2, CO_2, H_2O, CO, H_2, NO and OH [18,19].

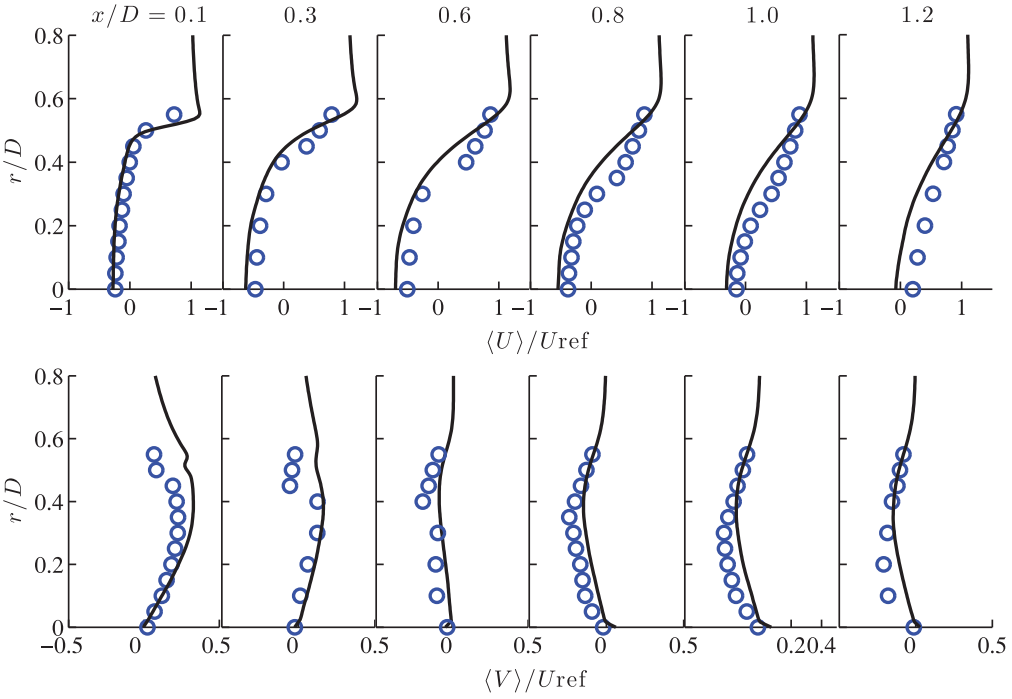

Fig. 14. Comparison of measured (symbols) [16,17] and computed (lines) radial variation of $\langle U \rangle / U_{ref}$ and $\langle V \rangle / U_{ref}$ for 24% TI case in flamelet combustion region marked as R1 and R2 in Fig. 12.

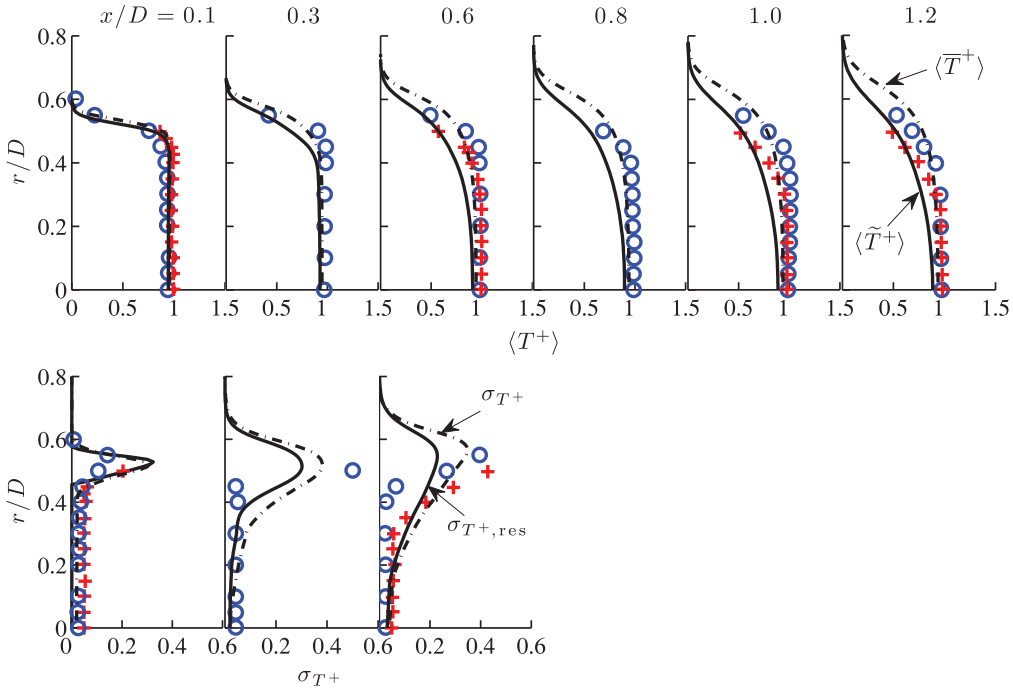

Fig. 15. Computed radial variation of normalised mean temperature and its rms (——) are compared with measurements using Rayleigh [18,19] (○○) and CARS [16] (+ +) techniques for 24% TI case in the region of flamelet combustion. Both σ_{T+} and $\sigma_{T+,\mathrm{res}}$ are shown.

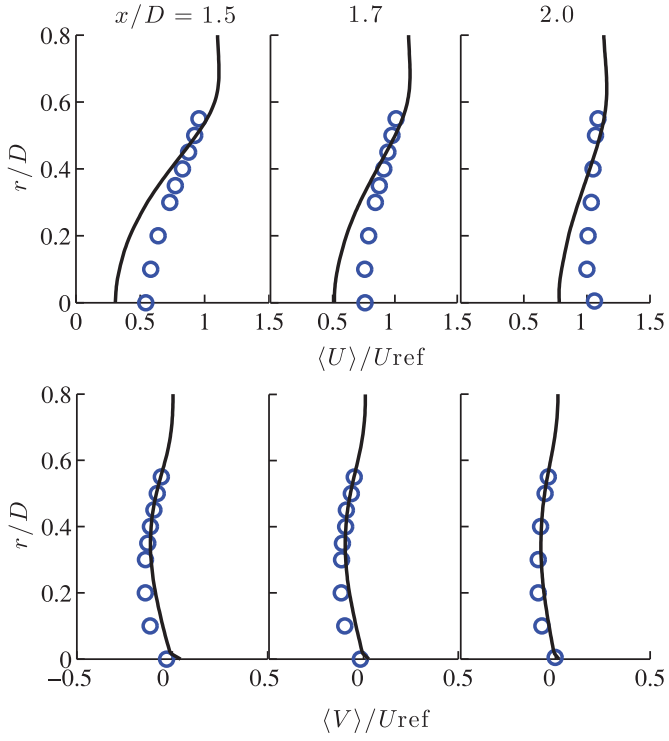

Fig. 16. Radial variations of $\langle U\rangle/U_{\mathrm{ref}}$ and $\langle V\rangle/U_{\mathrm{ref}}$ (——) are compared with measurements [16,17] (symbols) for 24% TI in the post-recirculation region.

Spontaneous Raman scattering was used for the first six species and Laser Induced Fluorescence (LIF) was used for OH and NO [18]. The species, except CO, NO and OH, mass fractions at $x/D = 6$ were found to be the equilibrium values and super equilibrium values were found for OH and CO in the measurements (sub-equilibrium for NO).

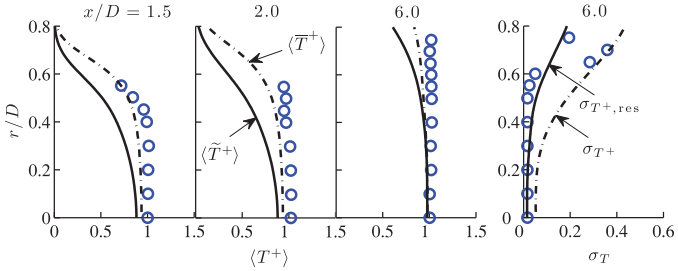

Fig. 17. Radial variations of normalised mean temperature and its rms in the post-recirculation region are compared with measurements [18,19] (symbols).

The mean mass fractions are post processed

$$\langle \overline{Y}_i \rangle = \langle \rho \rangle \int_0^1 \frac{Y_i}{\rho} \widetilde{P}(\zeta; \langle \widetilde{c} \rangle, \sigma_c^2) \quad \mathrm{d}\zeta, \tag{11}$$

which is similar to Eq. (2) except that the PDF above is not the sub-grid PDF. The PDF in the above equation involves the time-averaged statistics of the progress variable. One can compute the filtered mass fractions, $\overline{Y}_i$, using the sub-grid PDF first and then time averaged to yield $\langle \overline{Y}_i \rangle$. This procedure has to be followed within LES, which will incur additional computational expenses. Since the difference between $\langle \overline{Y}_i \rangle$ computed using the above two approaches is found to be small (not shown here) and the former approach saves some computational efforts, the results obtained using Eq. (11) are studied here. These mass fractions are compared to measurements in Figs. 18–21 along with the influence of c definition, which will be discussed in detail in Section 4.5.

The comparisons shown for $\langle \overline{Y}_{\mathrm{CH_4}} \rangle$ and $\langle \overline{Y}_{\mathrm{O_2}} \rangle$ in Fig. 18 are very good for all streamwise locations considered. These results are also shown for distributed combustion region downstream of the recirculation zone. The methane mass fraction can also be computed as $\langle \overline{Y}_{\mathrm{CH_4}} \rangle = (1 - \langle \overline{c} \rangle) Y^u_{\mathrm{CH_4}}$ using the definition of c and these values (not shown) compare well with those obtained using Eq. (11). The predictions of $\langle \overline{Y}_{\mathrm{CO_2}} \rangle$ and $\langle \overline{Y}_{\mathrm{H_2O}} \rangle$ are compared in Fig. 19 and

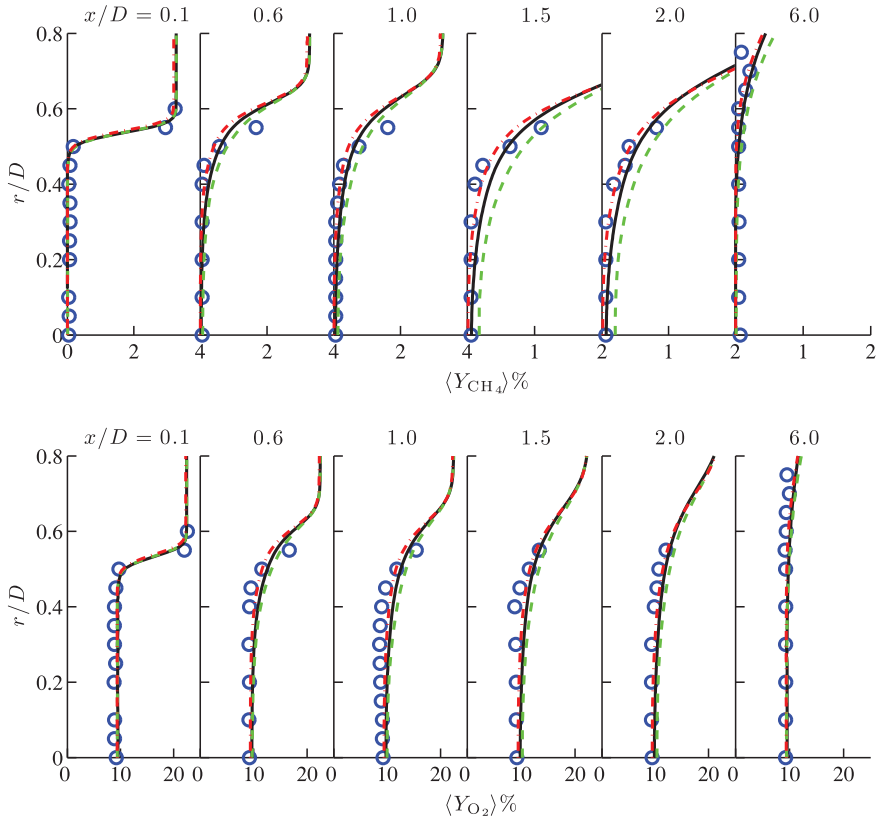

Fig. 18. Comparison of measured [18,19] (symbols) and computed time-averaged mass fractions of CH_4 and O_2 using $c = 1 - Y_{CH4}/Y^u_{CH_4}$ (——), $c_1 = Y_{H_2O}/Y^b_{H_2O}$ (– –) and $c_2 = (Y_{CO_2} + Y_{CO})/(Y^b_{CO_2} + Y^b_{CO})$ (– · –) for six axial locations.

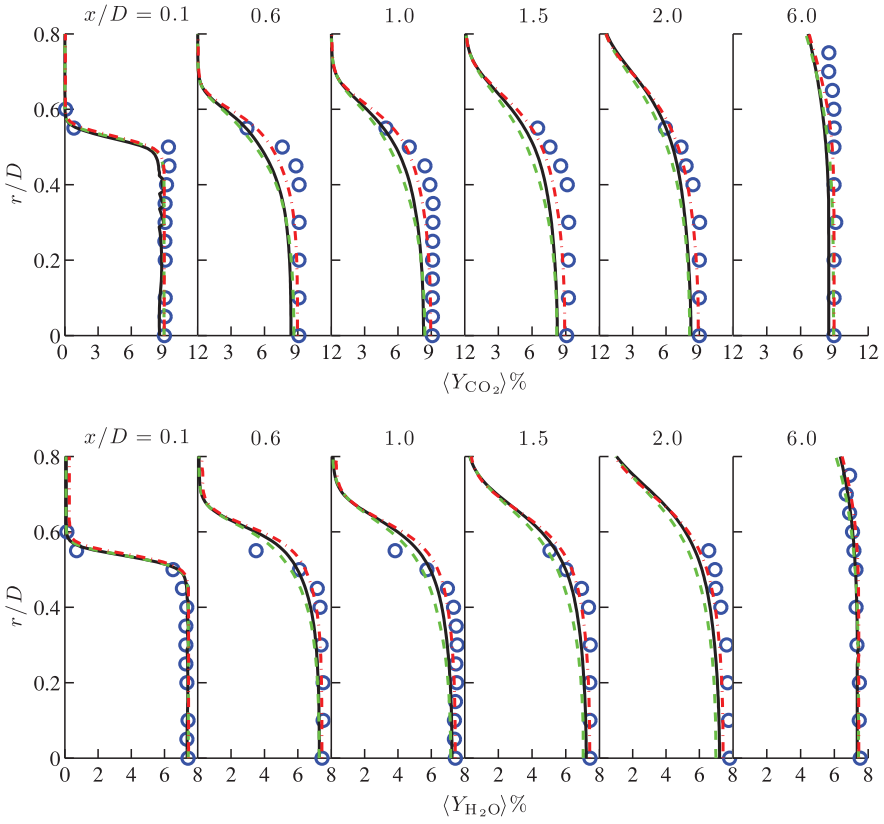

Fig. 19. Comparison of measured [18,19] (symbols) and computed time-averaged mass fractions of CO_2 and H_2O using $c = 1 - Y_{CH4}/Y^u_{CH_4}$ (——), $c_1 = Y_{H_2O}/Y^b_{H_2O}$ (– –) and $c_2 = (Y_{CO_2} + Y_{CO})/(Y^b_{CO_2} + Y^b_{CO})$ (– · –) for six axial locations.

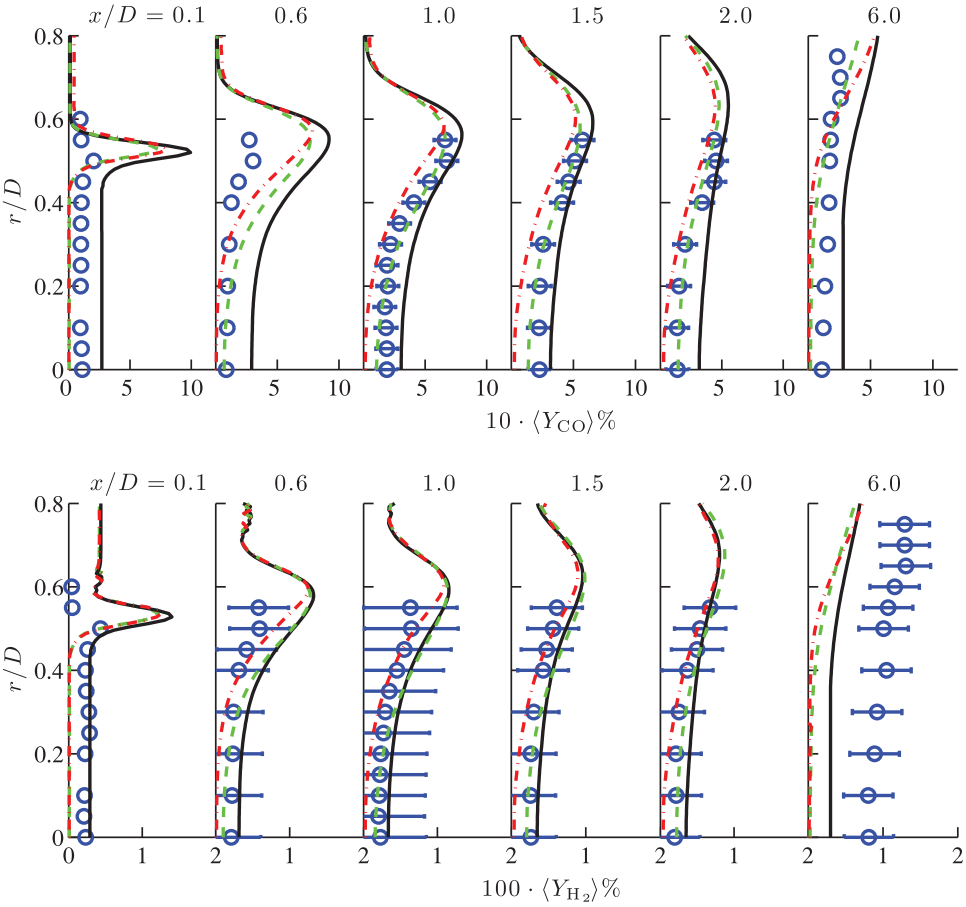

Fig. 20. Comparison of measured [18,19] (symbols) and computed time-averaged mass fractions of CO and H_2 using $c = 1 - Y_{CH4}/Y^u_{CH_4}$ (——), $c_1 = Y_{H_2O}/Y^b_{H_2O}$ (– –) and $c_2 = (Y_{CO_2} + Y_{CO})/(Y^b_{CO_2} + Y^b_{CO})$ (– · –) for six axial locations.

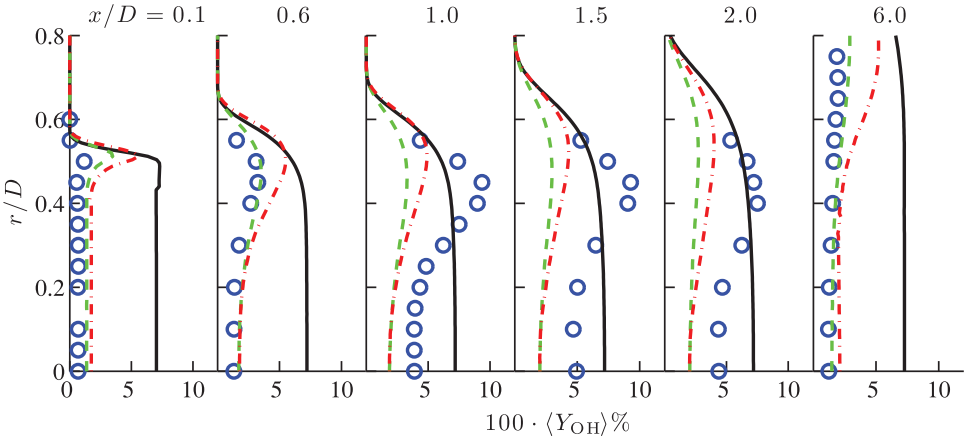

Fig. 21. Comparison of measured [18,19] (symbols) and computed time-averaged mass fraction of OH using $c = 1 - Y_{CH4}/Y^u_{CH_4}$ (——), $c_1 = Y_{H_2O}/Y^b_{H_2O}$ (– –) and $c_2 = (Y_{CO_2} + Y_{CO})/(Y^b_{CO_2} + Y^b_{CO})$ (– · –) for six axial locations.

the predictions are good for water mass fraction. There is, however, some under prediction (solid line) for CO_2 which is related to the definition of c and further insights are given in Section 4.5. The equilibrium value at $x/D = 6$ is also well captured in the LES. Overall, the agreement shown is very good for the major species.

The results for intermediates and a minor species are shown in Figs. 20 and 21, respectively. The error bars are shown when the measurement error is larger than the symbol size. There is substantial over prediction of CO for upstream positions and comparison with the measurements improve as one moves downstream. However, the final equilibrium value is over estimated. These behaviours are similar to that observed in earlier studies [6,49] on Bunsen flames suggesting that a flamelet parameterised using major species may be inadequate to capture the CO variation since its time scale is relatively larger and, this can be partially taken into account by using an appropriate definition for c as discussed in the next subsection. Alternatively, one can transport CO in the LES or use unsteady flamelet, which are to be explored in a future study. The predicted H_2 mass fractions are well within the error bars except for $x = 6\,D$ location. The OH mass fractions in the

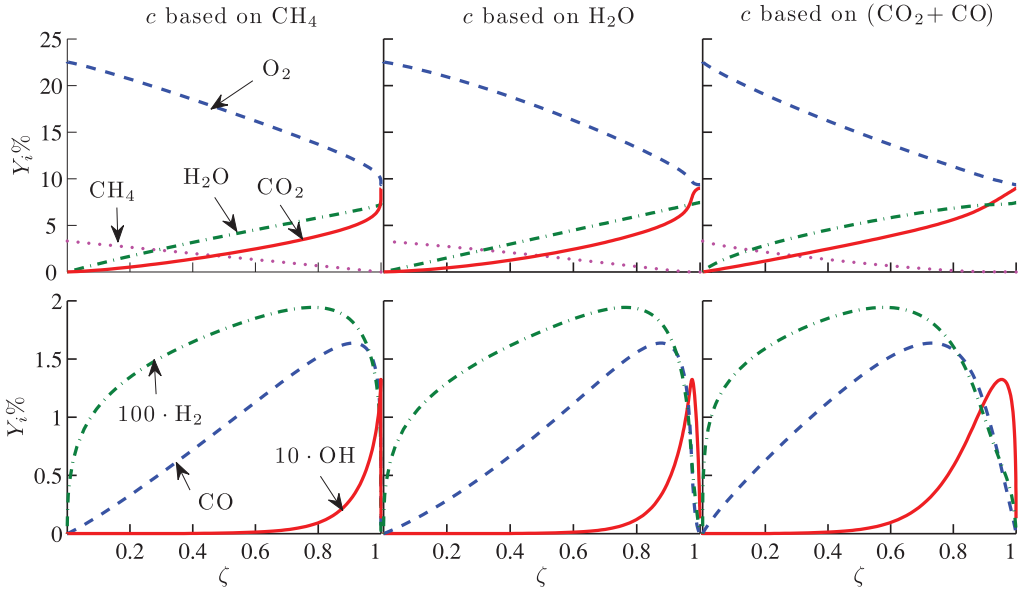

Fig. 22. Variations of major and minor species mass fractions with different definitions of progress variable.

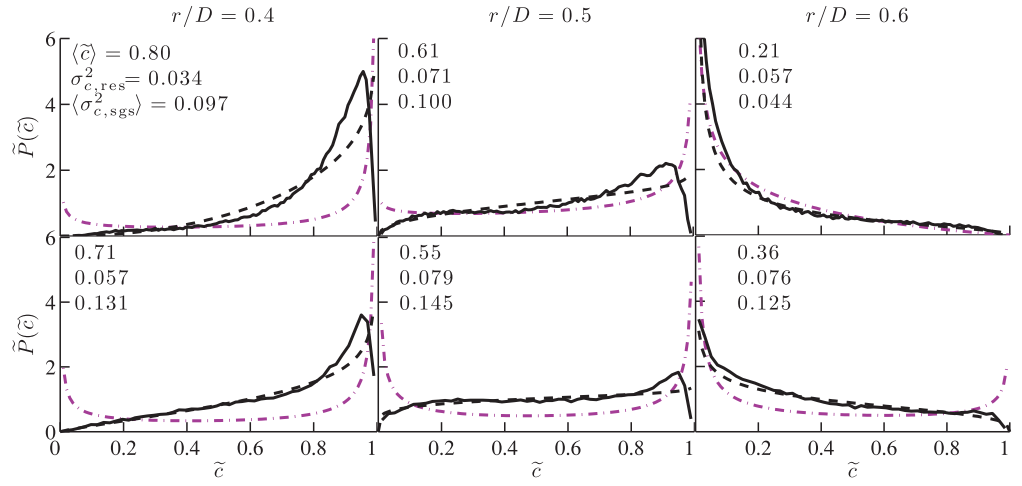

Fig. 23. Favre PDF of $\widetilde{c}$ from LES (——) at two axial locations $x/D = 0.6$ (top row) and $x/D = 2.0$ (bottom), and three radial positions of $r/D = 0.4$, 0.5 and 0.6. The time-averaged progress variable $\langle\widetilde{c}\rangle$ at these locations along with the corresponding resolved, $\sigma^2_{\widetilde{c},\mathrm{res}}$, and SGS, $\langle\sigma^2_{\widetilde{c},\mathrm{sgs}}\rangle$, variances are given. The dashed line is the β-PDF obtained using $\langle\widetilde{c}\rangle$ and $\sigma^2_{\widetilde{c},\mathrm{res}}$. The dash-dotted line is the β-PDF obtained using $\langle\widetilde{c}\rangle$ and $\langle\sigma^2_{\widetilde{c},\mathrm{sgs}}\rangle$.

flame regions $0.35 \le r/D \le 0.6$ are predicted reasonably well for locations $x/D = 1$, 1.5 and 2. However, the burnt side values inside the recirculation region and for $x/D = 6$ location are over estimated severely (solid lines), which is related to the choice of c definition.

4.5. Sensitivity to the choice of progress variable

The progress variable is defined using CH_4, see Eq. (8), for the above analysis. One can also define c using other species as

$$c_1 = \frac{Y_{H_2O}}{Y^b_{H_2O}} \quad \text{and} \quad c_2 = \frac{(Y_{CO_2} + Y_{CO})}{\left(Y^b_{CO_2} + Y^b_{CO}\right)} \tag{12}$$

where the superscript b refers to the burnt mixture value. The definition employed for c_2 has also been used in the past [53–57]. Figure 22 shows the variation of flamelet mass fractions, $Y_i(\zeta)$, of major and minor species with ζ for the three definitions of c. Gradients of Y_{CO}, Y_{CO_2} and Y_{OH} are very strong near $\zeta = 1$ for the methane-based progress variable. This strong gradient will cause numerical issues while evaluating the integral in Eq. (11) and the severity is reduced for c_1 and this is not an issue for c_2.

If $\sigma_c^2 \to 0$ then $\widetilde{c} \to \zeta$ and $\langle\overline{Y}_i\rangle \to Y_i(\zeta)$. Under this condition (specifically for the burnt side temperature), an error of 0.01% in ζ will produce an error of 90% in Y_{OH}. The value of $\langle c\rangle$ is expected to be 1 for $x/D = 0.1$ and $r/D = 0$ but the computed value is $\langle c\rangle \approx 0.9998$, which is comparable to 1. However this 0.02% error can yield more than 300% error yielding poor prediction of OH mass fraction (solid lines) seen in Fig. 21. This also applies to CO and H_2 mass fractions in the burnt mixtures. When the progress variable c_1 or c_2 is used the computed mean mass fractions agree well with the measurements, except for H_2 mass fraction at location $x/D = 6$. Overall, the major species mean mass fractions are insensitive to the choice of c but the minor and intermediate species are sensitive and it seems that c based on $(CO + CO_2)$ is a good choice for the flames investigated here. This sensitivity is large for minor species exhibiting large gradients near the burnt side of the flamelet (see Fig. 22), indicating that the most of this sensitivity comes from the numerical issues because of this gradient as noted earlier. A small sensitivity observed for major species could result from some difference in the fields of local reaction rate and density for different progress variable

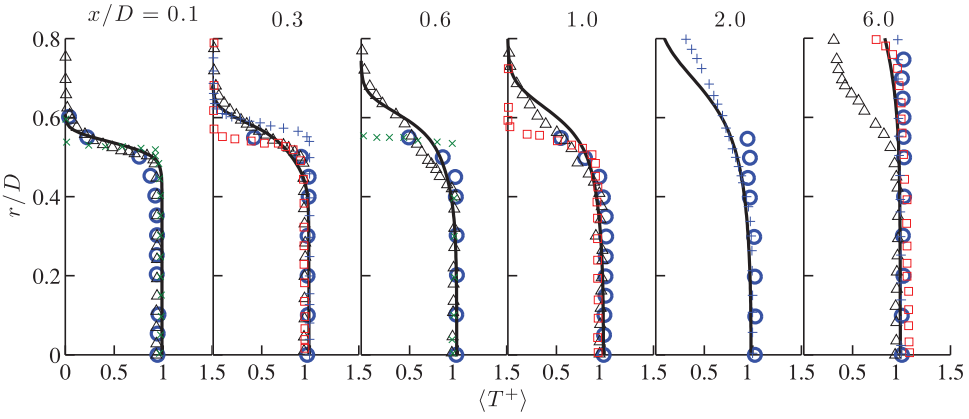

Fig. A1. Comparison of measured [18,19] (circles) and computed time-averaged temperature: present study (solid line), [20] (×), [21] (△), [22] (+) and [29] (□).

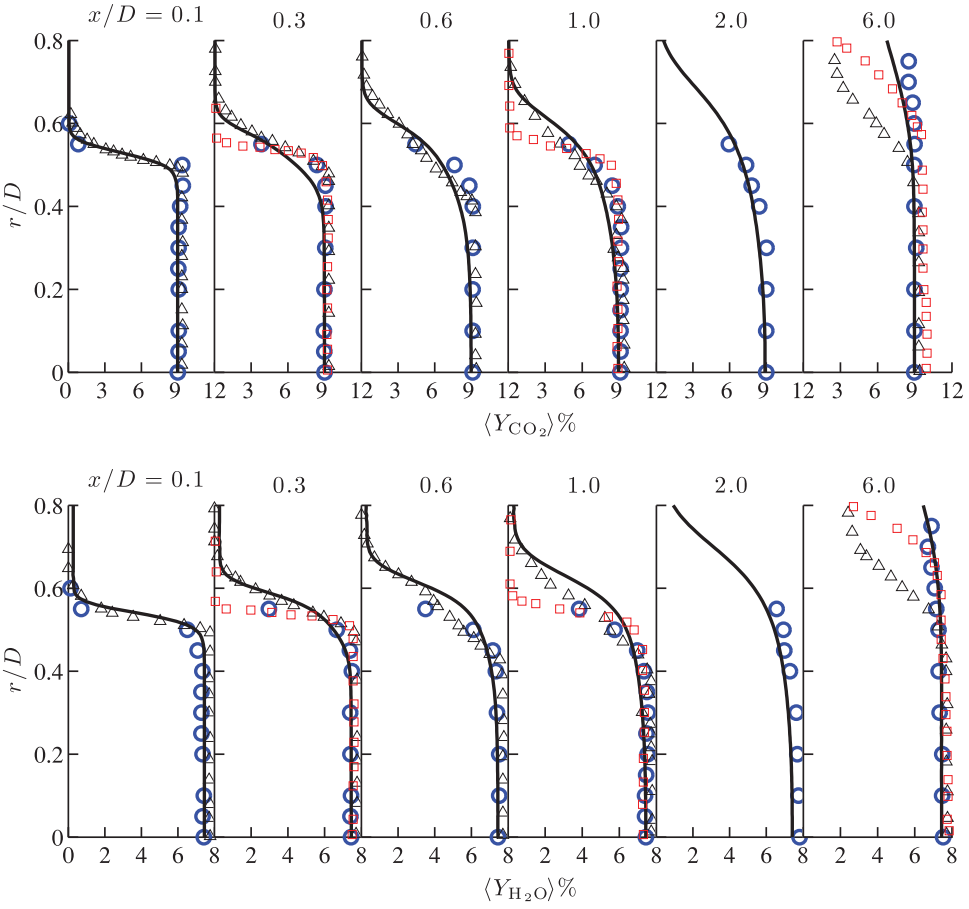

Fig. A2. Comparison of measured [18,19] (circles) and computed time-averaged mass fractions of CO_2 and H_2O: present study (solid line), [21] (△) and [29] (□).

definitions. However, this sensitivity is observed to be negligibly small.

4.6. PDF of progress variable

The PDFs of the progress variable are shown in Fig. 23 for three radial locations at two axial positions and these locations are chosen to cover the flame brush. The density weighted time-averaged progress variable, resolved and sub-grid variances are given in the figure. These statistics are obtained using 450 snapshots of three dimensional data sampled over about 180 ms and these snapshots are separated by about 0.4 ms. Three curves are shown for each location. The solid line is the PDF from LES constructed using $\widetilde{c}$ and the corresponding Beta PDF obtained with $\langle\widetilde{c}\rangle$ and $\sigma^2_{c,\mathrm{res}}$ is shown using the dashed line. A good agreement observed suggests that the resolved field PDF is captured well by the Beta function and this PDF is monomodal. The broad distribution seen for $r/D = 0.5$ suggests a broad flame brush. If one is interested in comparison with the experimental PDF of c then the total variance, $\sigma^2_{c,\mathrm{res}} + \langle\sigma^2_{c,\mathrm{sgs}}\rangle$, must be used for the Beta PDF.

The dashed dotted line is the Beta PDF constructed using $\langle\widetilde{c}\rangle$ and $\langle\sigma^2_{c,\mathrm{sgs}}\rangle$. Thus, this PDF is for the subgrid processes. The time-averaged SGS variance, $\langle\sigma^2_{c,\mathrm{sgs}}\rangle$, is typically larger than $\sigma^2_{c,\mathrm{res}}$ as noted earlier in Fig. 6. Thus, this PDF is typically bimodal except for locations where reaction rate is expected to be very low, see for example the PDF at $r/D = 0.6$ with $\langle\widetilde{c}\rangle = 0.21$ shown

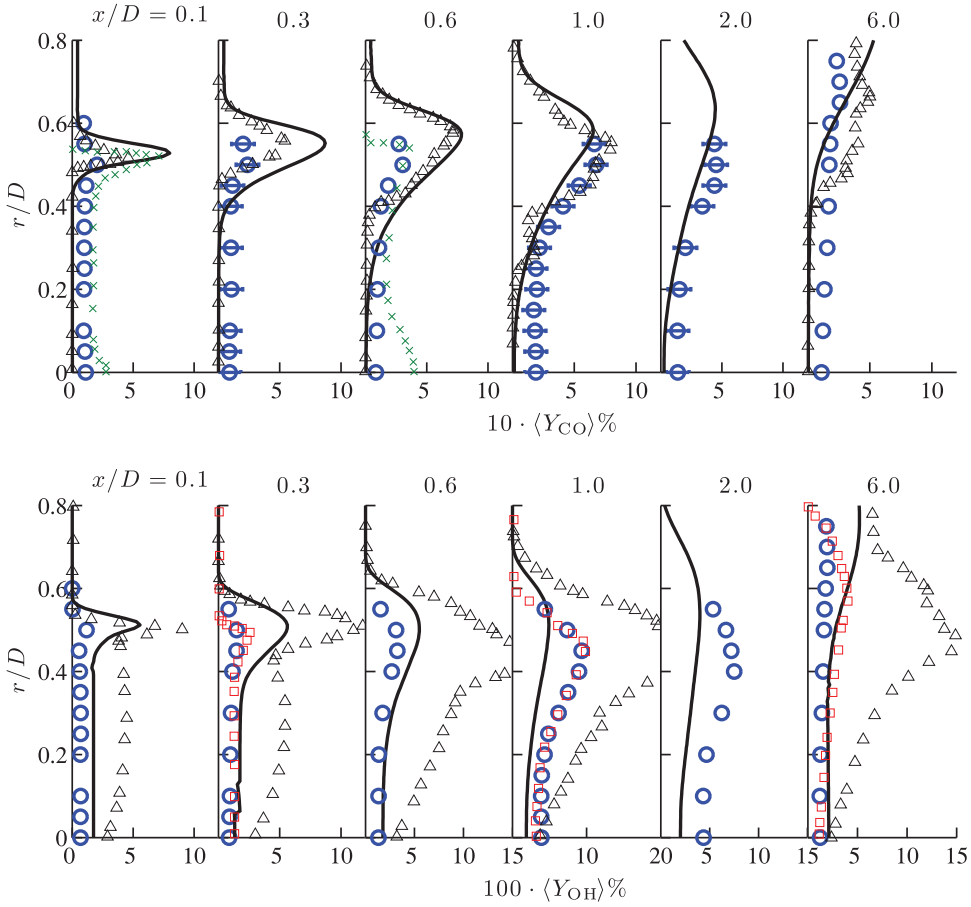

Fig. A3. Comparison of measured [18,19] (circles) and computed time-averaged mass fractions of CO and OH: present study (solid line), [20] (×), [21] (△) and [29] (□).

in Fig. 23. The bimodal behaviour is strong for locations with large reaction rate and thus this behaviour suggests that the combustion is flamelet-like. The presence of flamelets in distributed regime combustion has been observed in previous experimental (see for example [30,31,34,35]) and numerical (see for example [4,58,59]) studies. Thus, the good performance observed here for the unstrained flamelet model is not surprising. Furthermore, the distributed combustion may have to be seen as a regime where (continuous or broken) flamelets with structures unperturbed by turbulent eddies are distributed over a larger region yielding a thick and diffusive flame brush. In the classical viewpoint, large-scale turbulence has scales smaller than the laminar flame scales and so the turbulence can disturb the flamelet structure in both preheat and reaction zones. This would also give a thick flame brush and there is not enough evidence in the literature to support this classical viewpoint, but there are ample evidences to support the alternative viewpoint expressed above.

5. Summary & Conclusion

Turbulent lean premixed methane-air flames stabilised behind a bluff-body are simulated using LES and, the results are analysed and compared to measurements. The filtered reaction rate is modelled using unstrained flamelet with a presumed subgrid PDF for reaction progress variable. This closure needs a model for the subgrid variance and its dissipation rate. The former is obtained using its transport equation to include all the relevant physical processes while the latter is modelled using an algebraic closure with its scale dependent parameter evaluated dynamically. The commonly used algebraic model for the SGS variance and a linear relaxation model involving SGS flow time scale for the dissipation rate are shown to be inadequate, which was also shown for piloted Bunsen flames in another study [6]. If the various closures involved are physically consistent with one another then the unstrained flamelet model performs well for multi-regime combustion as shown here and in a previous study [6].

Comparisons of cold flow statistics from LES with those from measurements demonstrate that the model setup, boundary conditions and numerical grid used represents the experimental conditions well. The reacting flow results show that the mean axial velocity is sensitive to the level of approach turbulence while the mean temperature has reduced sensitivity to this parameter as observed in the measurements. The recirculation zone length and mean flow velocities are captured well. The time-averaged temperature is captured quite well for both flames with 2% and 24% turbulent intensity. The subgrid variance of normalised temperature is approximated to be the same as the subgrid variance of mass fraction based progress variable because the Lewis number is unity for the lean methane–air mixture. The predictions of mean mass fractions of various species agree well with measurements if the progress variable is chosen carefully to avoid numerical error while constructing the lookup table. This error is quite significant for fuel based progress variable. The subgrid PDF of progress variable is observed to be bimodal even in regions expected to have distributed combustion characteristics and this supports the good performance of the flamelet model shown in this paper. In summary, the unstrained flamelet closure with physically consistent closures for subgrid variance of progress variable and its dissipation rate is shown to work well for a quite common burner con-

figuration for practical combustors. However, further assessment of this model's capabilities for more complex flow and flame configurations, for example swirling flames, is required to establish its robustness and accuracy. This will be investigated in future works.

Acknowledgment

The authors express their gratitude to EPSRC, Siemens and Rolls-Royce for their support. This work is funded by the grant numbered EP/I027556/1. The numerical data used in this study may be obtained by contacting the corresponding author.

Appendix A. Typical comparisons with previous LES studies

The current LES results for the 24% IT case are compared with previous LES results along with measurements in this Appendix to show the relative performance of different combustion models. The results obtained using the unstrained flamelet model in this study for the progress variable based on $CO_2 + CO$ are compared with those in [20–22,29]. Hu & Correa [20] used a presumed PDF approach with perfectly stirred reactor library and Cannon et al. [21] performed 2D LEM-LES computations. Andreini et al. [22] compared different combustion models available in commercial softwares and their LES results using Zimont's model available in Fluent are used for comparison here. Liu et al. [29] used a transported PDF method for their calculations. All these models have their advantages and limitations and it is worth to note that the computational cost for presumed PDF methods is significantly lower than that for LEM-LES and transported PDF methods. Typical comparisons are shown for temperature, two major and two minor species at various axial locations reported in the previous studies cited above.

Although the results of unstrained flamelet model compare well with those in previous studies, they seem to show improved accuracy in comparison to computationally expensive models like LEM-LES or transported PDF. A complete assessment of the relative accuracy of the results in this study with those in [20] and [22] cannot be done because of the very limited data available in those works. It is worth noting that the modelling constants were selected carefully in both of these works [20,22]. A very good comparison is shown for OH mass fraction for the transport-PDF approach [29] but it is unclear how other minor species compared with measurements as they were not reported for the transport-PDF calculation.

References

[1] L.Y.M. Gicquel, G. Staffelbach, T. Poinsot, Large eddy simulations of gaseous flames in gas turbine combustion chambers, Prog. Energy Combust. Sci. 38 (2012) 782–817.
[2] H. Pitsch, Large-eddy simulation of turbulent combustion, Annu. Rev. Fluid Mech. 38 (2006) 453–482.
[3] N. Swaminathan, K.N.C. Bray, Fundamentals and challenges, in: N. Swaminathan, K.N.C. Bray (Eds.), Turbulent Premixed Flames, Cambridge University Press, Cambridge, UK (2011), pp. 1–40.
[4] E. Knudsen, H. Pitsch, Capabilities and limitations of multi-regime flamelet combustion models, Combust. Flame 159 (2012) 242–264.
[5] E. Knudsen, H. Kolla, E.R. Hawkes, H. Pitsch, LES of a premixed jet flame DNS using a strained flamelet model, Combust. Flame 160 (2013) 2911–2927.
[6] I. Langella, N. Swaminathan, Unstrained and strained flamelets for LES of premixed combustion, Combust. Theory Model. 20 (2016) 410–440.
[7] A. Sjunnesson, C. Nelsson, E. Max, LDA measurements of velocities and turbulence in a bluff body stabilized flame, Laser Anemomet. 3 (1991) 83–90.
[8] A. Sjunnesson, R. Henriksson, C. Lofstrom, CARS measurements and visualization of reacting flows in bluff body stabilized flame, AIAA Paper 92–3650.
[9] X. Bai, L. Fuchs, Modeling of turbulent reactive flows past a bluff body: assessment of accuracy and efficiency, Comput. Fluids 23 (1994) 507–521.
[10] C. Fureby, S.I. Möller, Large eddy simulation of reacting flows applied to bluff body stabilized flames, AIAA J. 33 (1995) 2339–2347.
[11] E. Giacomazzi, V. Battaglia, C. Bruno, The coupling of turbulence and chemistry in a premixed bluff-body flame as studied by LES, Combust. Flame 138 (2004) 320–335.
[12] I. Porumbel, S. Menon, Large eddy simulation of bluff body stabilized premixed, Flame, AIAA Paper 2006-152.
[13] T. Ma, O.T. Stein, N. Chakraborty, A.M. Kempf, A posteriori testing of algebraic flame surface density models for LES, Combust. Theory Modell. 17 (2013) 431–482.
[14] W.P. Jones, A.J. Marquis, F. Wang, Large eddy simulation of a premixed propane turbulent bluff body flame using the eulerian stochastic field method, Fuel 140 (2015) 514–525.
[15] J.C. Pan, M.D. Vangsness, S.P. Heneghan, D.R. Ballal, Laser diagnostic studies of bluff-body stabilized confined turbulent premixed flames, combustion fundamentals and applications: spring technical meeting: papers and programme, Combustion Institute, Central States Section (1991).
[16] J.C. Pan, M.D. Vangsness, S.P. Heneghan, D.R. Ballal, Scalar measurements in bluff body stabilized flames using CARS diagnostics, ASME 36th International Gas Turbine and Aeroengine Congress, Paper 91-GT-302 (1991).
[17] J.C. Pan, M.D. Vangsness, D.R. Ballal, Aerodynamics of bluff-body stabilized confined turbulent premixed flames, J. Eng. Gas Turb. Power 114 (1992) 783–789.
[18] S.P. Nandula, R.W. Pitz, R.S. Barlow, G.J. Fiechtner, Rayleigh/raman/LIF measurements in a turbulent lean premixed combustor, 34th Aerospace Sciences Meeting (1996). Paper AIAA–96–0937.
[19] S.P. Nandula, Lean premixed flame structure in intense turbulence: Rayleigh/Raman/LIF measurements and modeling, Vanderbilt University, Nashville, Tennessee, 2003 Ph.d. dissertation.
[20] I.Z. Hu, S.M. Correa, Calculations of turbulent flams using a perfectly stirred reactor library, Symp. (Int.) Combust. 26 (1996) 307–313.
[21] S. Cannon, B. Zuo, V. Adumitroaie, C.E. Smith, Linear eddy subgrid modeling of a lean premixed methane–air combustion, CFDRC, Pittsburg, PA (2002). Report No. 8321/8
[22] A. Andreini, C. Bianchini, A. Innocenzi, Large eddy simulation of a bluff body stabilized lean premixed flame, J. Combust. 2014 (2014) 710254.
[23] B.S. Brewster, S.M. Cannon, J.R. Farmer, F.L. Meng, Modeling of lean premixed combustion in stationary gas turbines, Prog. Energy Combust. Sci. 25 (1999) 353–385.
[24] N. Fueyo, W. Vicente, J. Blasco, C. Dopazo, Stochastic simulation of NO formation in lean premixed methane flames, Combust. Sci. Technol. 153 (2000) 295–311.
[25] W. Vicente, M. Salinas, E. Barrios, C. Dopazo, PDF modeling of CO and NO formation in lean premixed methane flames, Combust. Sci. Technol. 176 (2004) 585–601.
[26] W. Vicente, M. Salinas-Vázquez, E. Martínez, A. Rodríguez, Numerical simulation of a turbulent lean, premixed combustion with an explicit algebraic stress model, J. Math. Stat. 1 (2005) 86–90.
[27] J.R. Nanduri, D.R. Parson, S.L. Yilmaz, I.B. Celik, P.A. Strakey, Assessment of RANS-based turbulent combustion models for prediction of emissions from lean premixed combustion of methane, Combust. Sci. Technol. 182 (2010) 794–821.
[28] S.S. Sundaram, V. Babu, C. Obulesu, R. Sivakumar, Three-dimensional numerical simulation of turbulent, bluff-body stabilized, lean, premixed combustion, Combust. Sci. Technol. 184 (2012) 351–373.
[29] X. Liu, H. Zheng, J. Yang, Y. Li, LES-PDF modeling of blowout analysis in slit bluff-body stabilized flames, Int. J. Spray Combust. Dyn. 7 (2015) 131–150.
[30] M.J. Dunn, A.R. Masri, R.W. Bilger, A new piloted premixed jet burner to study strong finite-rate chemistry effects, Combust. Flame 151 (2007) 46–60.
[31] M.J. Dunn, A.R. Masri, R.W. Bilger, R.S. Barlow, G.H. Wang, The compositional structure of highly turbulent piloted premixed flames issuing into a hot coflow, Proc. Combust. Inst. 32 (2009) 1779–1786.
[32] M.J. Dunn, A.R. Masri, R.W. Bilger, R.S. Barlow, Finite rate chemistry effects in highly sheared turbulent premixed flames, Flow Turbul. Combust. 85 (2010) 621–648.
[33] A.Y. Poludnenko, E.S. Oran, The interaction of high-speed turbulence with flames: global properties and internal flame structure, Combust. Flame 157 (2010) 995–1011.
[34] W. Roberts, J. Driscoll, M. Drake, L. Goss, Images of the quenching of a flame by a vortex—to quantify regimes of turbulent combustion, Combust. Flame 94 (1993) 58–69.
[35] J.E. Temme, T.M. Wabel, A.W. Skiba, J.F. Driscoll, Measurements of premixed turbulent combustion regimes of high reynolds number flames, 53rd AIAA Aerospace Sciences Meeting (2015).
[36] M. Germano, U. Piomelli, P. Moin, W.H. Cabot, A dynamic subgrid-scale eddy viscosity model, Phys. Fluids A 3 (7) (1991) 1760.
[37] D. Lilly, A proposed modification of the germano subgrid scale closure method, Phys. Fluids A 4 (1992) 633–635.
[38] T.J. Poinsot, D. Veynante, Theoretical and numerical combustion, Edwards, 2005.
[39] T. Dunstan, Y. Minamoto, N. Chakraborty, N. Swaminathan, Scalar dissipation rate modelling for large eddy simulation of turbulent premixed flames, Proc. Combust. Inst. 34 (2013) 1193–1201.
[40] I. Langella, N. Swaminathan, Y. Gao, N. Chakraborty, Assessment of dynamic closure for premixed combustion LES, Combust. Theory Model. 19 (2015) 628–656.
[41] S.B. Pope, Turbulent flows, Cambridge University Press, 2000.
[42] Y. Gao, N. Chakraborty, N. Swaminathan, Dynamic closure of scalar dissipation rate for large eddy simulations of turbulent premixed combustion: a direct numerical simulations analysis, Flow Turbul. Combust. 95 (2015) 775–802.

[43] M.S. Anand, J. Zhu, C. Connor, M. Razdan, Combustor flow analysis using an advanced finite-volume design system, ASME International gas turbine and Aeroengine Congress and Exhibition (1999). Paper 99–GT–273
[44] J.P.V. Doormaal, G.D. Raithby, Enhancements of the simple method for predicting incompressible fluid flows, Numer. Heat Transf. 7 (1984) 147–163.
[45] S. Ruan, N. Swaminathan, O. Darbyshire, Modelling of turbulent lifted jet flames using flamelets: a priori assessment and a posteriori validation, Combust. Theory Model. 18 (2014) 295–329.
[46] R.J. Kee, J.F. Grcar, M.D. Smooke, J.A. Miller, A fortran program for modeling steady laminar one-dimensional premixed flames, Report No. SAND85-8240, Sandia National Labortories, CA, USA, 1985.
[47] M. Klein, M. Sadiki, J. Janicka, A digital filter based generation of inflow data for spatially developing direct numerical or large eddy simulations, J. Comput. Phys. 186 (2002) 652–665.
[48] I. Langella, N. Swaminathan, F.A. Williams, J. Furukawa, LES of premixed combustion in the corrugated-flamelet regime, Combust. Sci. Technol. (2016), doi:10.1080/00102202.2016.1195824.
[49] H. Kolla, N. Swaminathan, Strained flamelets for turbulent premixed flames II: laboratory flame results, Combust. Flame 157 (2010) 1274–1289.
[50] K. Bray, J. Moss, A unified statistical model of the premixed turbulent flame, Acta Astronaut. 4 (1977) 291–319.
[51] P. Libby, K. Bray, J. Moss, Effect of finite reaction rate and molecular transport in premixed turbulent combustion, Combust. Flame 34 (1979) 285–301.
[52] C.K. Law, Combustion physics, Cambridge University Press, New York, 2006.
[53] O. Gicquel, N. Darabiha, D. Thevenin, Liminar premixed hydrogen/air counterflow flame simulations using flame prolongation of ILDM with differential diffusion, Proc. Combust. Inst. 28 (2000) 1901–1908.
[54] B. Fiorina, R. Baron, O. Gicquel, D. Thevenin, S. Carpentier, N. Darabiha, Modelling non-adiabatic partially premixed flames using flame-prolongation of ILDM, Combust. Theory Model. 7 (2003) 449–470.
[55] P. Domingo, L. Vervisch, S. Payet, R. Hauguel, DNS of a premixed turbulent v flame and LES of a ducted flame using a FSD-PDF subgrid scale closure with FPI-tabulated chemistry, Combust. Flame 143 (2005) 566–586.
[56] J. Galpin, A. Naudin, L. Vervisch, C. Angelberger, O. Colin, P. Domingo, Large-eddy simulation of a fuel-lean premixed turbulent swirl-burner, Combust. Flame 155 (2008) 247–266.
[57] P. Domingo, L. Vervisch, D. Veynante, Large-eddy simulation of a lifted methane jet flame in a vitiated coflow, Combust. Flame 152 (2008) 415–432.
[58] C. Meneveau, T. Poinsot, Stretching and quenching of flamelets in premixed turbulent combustion, Combust. Flame 86 (1991) 311–332.
[59] S. Srinivasan, S. Menon, Linear eddy mixing model studies of high karlovitz number turbulent premixed flames, Flow Turb. Combust. 93 (2014) 189–219.